The Astrophysical Journal, 933:10 (17pp), 2022 July 1 https://doi.org/10.3847/1538-4357/ac6e68

VERTICO II: How H I-identified Environmental Mechanisms Affect the Molecular Gas in Cluster Galaxies

Nikki Zabel[1], Toby Brown[2,3], Christine D. Wilson[3], Timothy A. Davis[4], Luca Cortese[5,6], Laura C. Parker[3], Alessandro Boselli[7], Barbara Catinella[5,6], Ryan Chown[3], Aeree Chung[8], Tirna Deb[1], Sara L. Ellison[9], María J. Jiménez-Donaire[10,11], Bumhyun Lee[12,13], Ian D. Roberts[14], Kristine Spekkens[15], Adam R. H. Stevens[16], Mallory Thorp[9], Stephanie Tonnesen[17], and Vicente Villanueva[18]

[1] Kapteyn Astronomical Institute, University of Groningen PO Box 800, NL-9700 AV Groningen, The Netherlands; zabel@astro.rug.nl
[2] Herzberg Astronomy and Astrophysics Research Centre, National Research Council of Canada, 5071 West Saanich Rd, Victoria, BC V9E 2E7, Canada
[3] Department of Physics & Astronomy, McMaster University, 1280 Main Street W, Hamilton, ON L8S 4M1, Canada
[4] School of Physics & Astronomy, Cardiff University, Queens Buildings, The Parade, Cardiff CF24 3AA, UK
[5] International Centre for Radio Astronomy Research, The University of Western Australia, 35 Stirling Hwy, 6009 Crawley, WA, Australia
[6] ARC Centre of Excellence for All Sky Astrophysics in 3 Dimensions (ASTRO 3D), Australia
[7] Aix-Marseille Université, CNRS, CNES, LAM, Marseille, France
[8] Department of Astronomy, Yonsei University, 50 Yonsei-ro, Seodaemun-gu, Seoul, 03722, Republic of Korea
[9] Department of Physics & Astronomy, University of Victoria, Finnerty Road, Victoria, BC V8P 1A1, Canada
[10] Observatorio Astronómico Nacional (IGN), C/Alfonso XII, 3, E-28014 Madrid, Spain
[11] Centro de Desarrollos Tecnológicos, Observatorio de Yebes (IGN), E-19141 Yebes, Guadalajara, Spain
[12] Korea Astronomy and Space Science Institute, 776 Daedeokdae-ro, Yuseong-gu, Daejeon 34055, Republic of Korea
[13] Kavli Institute for Astronomy and Astrophysics, Peking University, Beijing 100871, People's Republic of China
[14] Leiden Observatory, Leiden University, PO Box 9513, 2300 RA Leiden, The Netherlands
[15] Royal Military College of Canada, PO Box 17000, Station Forces, Kingston, ON K7K 7B4, Canada
[16] International Centre for Radio Astronomy Research, The University of Western Australia, 35 Stirling Hwy, 6009 Crawley, WA, Australia
[17] CCA, Flatiron Institute, 162 5th Ave, New York, NY 10010, USA
[18] Department of Astronomy, University of Maryland, College Park, MD 20742, USA

Received 2022 January 18; revised 2022 May 3; accepted 2022 May 9; published 2022 June 28

Abstract

In this VERTICO early science paper we explore in detail how environmental mechanisms, identified in H I, affect the resolved properties of molecular gas reservoirs in cluster galaxies. The molecular gas is probed using ALMA ACA (+TP) observations of ^{12}CO(2–1) in 51 spiral galaxies in the Virgo cluster (of which 49 are detected), all of which are included in the VIVA H I survey. The sample spans a stellar mass range of $9 \leqslant \log M_\star/M_\odot \leqslant 11$. We study molecular gas radial profiles, isodensity radii, and surface densities as a function of galaxy H I deficiency and morphology. There is a weak correlation between global H I and H_2 deficiencies, and resolved properties of molecular gas correlate with H I deficiency: galaxies that have large H I deficiencies have relatively steep and truncated molecular gas radial profiles, which is due to the removal of low-surface-density molecular gas on the outskirts. Therefore, while the environmental mechanisms observed in H I also affect molecular gas reservoirs, there is only a moderate reduction of the total amount of molecular gas.

Unified Astronomy Thesaurus concepts: Galaxies (573); Virgo Cluster (1772); Interstellar medium (847); Molecular gas (1073); Galaxy clusters (584); Galaxy evolution (594); Galaxy environments (2029)

1. Introduction

Hosting hundreds to thousands of galaxies bound by a dark matter halo, galaxy clusters form the largest virialized structures in the Universe. In these high-density environments, galaxies evolve differently from their isolated counterparts, with galaxy clusters in the local Universe typically harboring a much higher fraction of passive galaxies than the field population (e.g., Oemler 1974; Dressler 1980; Goto et al. 2003). This implies that some galaxies residing in clusters slow down ("quench") their star formation relatively quickly. Various environmental processes are known to be able to contribute to this premature quenching, such as ram pressure stripping (RPS, Gunn & Gott 1972, see also Cortese et al. 2021 and Boselli et al. 2021 for recent reviews), the lack of fresh gas available for accretion, e.g., from the circum-galactic medium, causing a galaxy to deplete its gas reservoir (also referred to as "starvation," Larson et al. 1980), galaxy-galaxy interactions (Moore et al. 1996), tidal interactions, and thermal evaporation and viscous stripping (Cowie & Songaila 1977; Nulsen 1982, see also Cortese et al. 2021 for extensive descriptions of each environmental mechanism). The relative importance of these mechanisms, and to which extent this varies between clusters, is not yet well-understood.

Typically distributed within an extended disk ($D_{\rm H\,I} \sim 1-2\,D_{25}$, e.g., Verheijen & Sancisi 2001) and relatively loosely bound, atomic gas (H I) is susceptible to environmental processes. Cluster galaxies are often H I deficient (i.e., they contain less H I than expected from their optical size), and have truncated and/or asymmetric H I disks (e.g., Haynes et al. 1984; Giovanelli & Haynes 1985; Cayatte et al. 1990; Schröder et al. 2001; Solanes et al. 2001; Waugh et al. 2002; Gavazzi et al. 2005; Rasmussen et al. 2006; Chung et al. 2009; Hughes & Cortese 2009; Odekon et al. 2016; Yoon et al. 2017; Loni et al. 2021). Since atomic gas provides the fuel for molecular clouds, which will eventually collapse into stars, this removal of H I might lead to the quenching of star formation.

More recently, it has been shown that, despite its more tightly bound and centrally located nature (e.g., Davis et al. 2013), molecular gas can also be *directly* affected by environmental processes. For example, molecular gas disks in cluster galaxies have been found to be truncated and/or morphologically and kinematically disturbed, while molecular gas fractions have been found to be deficient compared to field galaxies at fixed stellar mass (e.g., Vollmer et al. 2008; Fumagalli et al. 2009; Boselli et al. 2014a; Lee et al. 2017; Lee & Chung 2018; Zabel et al. 2019; Cramer et al. 2021; Brown et al. 2021). Additionally, molecular gas fractions can also be *enhanced* in cluster galaxies, as a result of ram pressure, which can facilitate the conversion of atomic into molecular gas (e.g., Moretti et al. 2020).

It is not yet clear to what extent the processes acting on the atomic gas also affect the molecular gas and, if they do, on what relative timescales. It is possible that (a) atomic and molecular gas are removed and disturbed simultaneously by the same environmental processes (for example by galaxy-galaxy interactions), (b) the majority of the atomic gas is removed before the molecular gas (for example by RPS), or (c) atomic and molecular gas are affected by different environmental processes entirely (for example, molecular gas is depleted through starvation while atomic gas is being stripped). Which of these options is closest to reality has strong implications for the process of environmental quenching, and the timescales on which this takes place.

Whether the molecular gas reservoirs of Virgo galaxies are different from those of their counterparts in the field has been a matter of debate (Stark et al. 1986; Kenney & Young 1989; Boselli et al. 1995; Mok et al. 2016, 2017). Boselli et al. (2014a) studied the H_2 content of ∼75 spiral galaxies in the Virgo cluster using the Herschel Reference Survey (HRS, Boselli et al. 2010) and compared them to the remaining field galaxies in the HRS. They find that, on average, H I-deficient Virgo cluster galaxies have less molecular gas than H I-normal field galaxies. Moreover, they find a weak but statistically significant increase in H_2 deficiency as a function of H I deficiency. This suggests that both gas phases are affected simultaneously in the Virgo cluster. Resolved observations of 17 of these HRS Virgo galaxies (Kuno et al. 2007) show a decrease in the extent of the molecular gas disk with increasing H I deficiency, which implies outside-in stripping of the molecular gas. On the other hand, Loni et al. (2021) find significant scatter in H_2/H I mass ratios in galaxies in the Fornax cluster (including both upper and lower limits), suggesting that the relative effects of environmental mechanisms on both gas phases are not straightforward.

This work is one of the early science papers of the Atacama Large Millimeter/submillimeter Array (ALMA) large program the "Virgo Environment Traced in CO" (VERTICO, Brown et al. 2021, hereafter referred to as B21). VERTICO comprises homogeneous CO(2-1) observations of 51 spiral galaxies in the Virgo cluster (of which 49 are detected), and is designed to systematically study the physical mechanisms that drive galaxy evolution in dense environments. Because the VERTICO sample is selected from the Very Large Array Imaging of Virgo in Atomic gas survey (VIVA, Chung et al. 2009, see Section 2), ancillary H I imaging is available for all CO-detected galaxies in the sample. In this work, we study the resolved atomic and molecular gas in the 49 Virgo galaxies detected in CO with VERTICO.

The Virgo cluster is a young and dynamically active cluster, with several substructures and infalling groups (e.g., Gavazzi et al. 1999; Solanes et al. 2002; Boselli et al. 2014b; Lisker et al. 2018). As the closest galaxy cluster to us (at ∼16.5 Mpc, Mei et al. 2007), it has been studied extensively in a range of wavelengths (Binggeli et al. 1985; McLaughlin 1999; Fouqué et al. 2001; Davies et al. 2010; Boselli et al. 2011, 2018; Ferrarese et al. 2012; Mihos et al. 2017, see also the references in B21). Following B21, we adopt a common distance of 16.5 Mpc for all galaxies in the sample.

In this work, we study how molecular gas is affected by environment in galaxies in the Virgo cluster. We make use of the homogeneity and resolution of VERTICO to study resolved properties of the molecular gas, such as sizes and radial profiles, and compare them to those of control galaxies. We probe the extent to which a galaxy is affected by environment, and the mechanism by which it is affected (if it is possible to identify this), using H I data from the VIVA survey (Chung et al. 2009; Yoon et al. 2017).

This paper is organized as follows. In Section 2, the sample, observations, and data reduction are described. The control samples used to compare our results to are introduced here. Section 3 contains the methods used, as well as a description of various definitions adopted throughout this work. Deficiency parameters are defined for both the atomic and molecular gas, and the calculation of radial profiles, H_2 radii, and median H_2 surface densities is also described here. In Section 4, we describe the results, and provide brief interpretations, while in Section 5, we provide a more thorough interpretation and discussion, including comparison to previous work. Finally, a short summary, as well as an itemized list of the findings from this work, are given in Section 6.

2. Sample, Observations, and Data Reduction

The sample used in this work consists of the 49 CO-detected VERTICO galaxies. The sample selection and data reduction of VERTICO are described in detail in B21, and are summarized below.

VERTICO targeted the CO(2-1) line in 51 late-type galaxies that were part of the VIVA survey (Chung et al. 2009) using the ALMA Atacama Compact Array (ACA). Of these, 15 galaxies that were already observed with the ACA were taken from the ALMA archive. Archival galaxies primarily come from the ALMA component of the Physics at High Angular resolution in Nearby Galaxies project (PHANGS-ALMA; Leroy et al. 2021a, various project IDs; see Table 2 in that work). One galaxy, NGC4402, comes from (Cramer et al. 2020, project ID 2016.1.00912.S). The final sample includes galaxies undergoing a variety of environmental effects, as identified in their H I imaging (Chung et al. 2009). Our sample spans a stellar mass range of $10^9 \leqslant M_\star/M_\odot \leqslant 10^{11}$. B21 calculated inclination and position angles from fits to Sloan Digital Sky Survey (SDSS, York et al. 2000; Alam et al. 2015) *r*-band images (see Table 1 in B21).

The 36 galaxies that were not yet on the ALMA archive were observed during Cycle 7 under program ID 2019.1.00763.L. Total Power (TP) observations were added for 25 targets for which the CO was expected to extend beyond the largest recoverable angular size of 29″.

For the 36 Cycle-7 galaxies, we used the calibrated UV data as delivered by ALMA. The raw UV data of the remaining 15 objects were recalibrated using the Common Astronomy Software Applications package (CASA, McMullin et al. 2007), using the

Table 1
Cold Gas Properties of The VERTICO Sample

Galaxy - (1)	R.A. (J2000) - (2)	Decl. (J2000) - (3)	$v_{\rm opt}$ km s^{-1} (4)	log $M_\star$ $M_\odot$ (5)	$R_\star$ kpc (6)	cl. - (7)	log $M_{\rm H\,I}$ $M_\odot$ (8)	def $_{{\rm H\,I},R_\star}$ dex (9)	def $_{{\rm H\,I},M_\star}$ dex (10)	log $M_{\rm mol}$ $M_\odot$ (11)	def $_{\rm H_2}$ dex (12)
IC3392	$12^{\rm h}28^{\rm m}43^{\rm s}.27$	14°59′57.″48	1678	9.51 ± 0.1	8.6	III	7.63 ± 0.35	1.15 ± 0.12	$1.50^{+0.02}_{-0.02}$	8.73 ± 0.02	$-0.13^{+0.02}_{-0.01}$
IC3418	$12^{\rm h}29^{\rm m}43^{\rm s}.92$	11°24′16.″88	38	8.37	-	-	$\leqslant 6.9$	-	$\geqslant -1.3$	$\leqslant 7.44$	$\geqslant -0.003$
NGC4064	$12^{\rm h}04^{\rm m}11^{\rm s}.26$	18°26′39.″12	1000	9.47 ± 0.1	18	III	7.6 ± 0.26	1.79 ± 0.2	$1.50^{+0.01}_{-0.02}$	8.41 ± 0.02	$-0.22^{+0.01}_{-0.10}$
NGC4189	$12^{\rm h}13^{\rm m}47^{\rm s}.47$	13°25′34.″68	1995	9.75 ± 0.1	9.6	0	8.75 ± 0.06	0.25 ± 0.04	$0.63^{+0.07}_{-0.03}$	8.69 ± 0.01	$-0.24^{+0.07}_{-0.00}$
NGC4192	$12^{\rm h}13^{\rm m}48^{\rm s}.58$	14°53′57.″12	−118	10.78 ± 0.1	57	IV	9.63 ± 0.04	0.51 ± 0.2	$0.23^{+0.04}_{-0.03}$	9.26 ± 0.01	$0.37^{+0.20}_{-0.12}$
NGC4216	$12^{\rm h}15^{\rm m}54^{\rm s}.19$	13°08′54.″96	30	10.91 ± 0.1	38	IV	9.25 ± 0.09	0.76 ± 0.2	$0.70^{+0.02}_{-0.04}$	8.96 ± 0.01	$0.56^{+0.06}_{-0.19}$
NGC4222	$12^{\rm h}16^{\rm m}22^{\rm s}.56$	13°18′25.″20	225	9.45 ± 0.2	15	0	8.81 ± 0.1	0.32 ± 0.04	$0.28^{+0.02}_{-0.15}$	8.06 ± 0.03	$0.11^{+0.03}_{-0.31}$
NGC4254[a]	$12^{\rm h}18^{\rm m}49^{\rm s}.68$	14°25′05.″52	2453	10.52 ± 0.1	17	I	9.65 ± 0.04	-0.1 ± 0.02	$-0.03\ ^{+0.02}_{-0.06}$	9.88 ± 0.00	$-0.51^{+0.12}_{-0.02}$
NGC4293[a]	$12^{\rm h}21^{\rm m}13^{\rm s}.47$	18°23′03.″12	717	10.5 ± 0.1	19	III	7.43 ± 0.48	2.25 ± 0.2	$2.16^{+0.02}_{-0.09}$	8.86 ± 0.01	$0.49^{+0.09}_{-0.02}$
NGC4294	$12^{\rm h}21^{\rm m}17^{\rm s}.81$	11°30′39.″24	421	9.38 ± 0.1	17	I	9.21 ± 0.03	-0.11 ± 0.02	$-0.18\ ^{+0.02}_{-0.12}$	7.75 ± 0.07	$0.28^{+0.08}_{-0.18}$
NGC4298[a]	$12^{\rm h}21^{\rm m}33^{\rm s}.12$	14°36′19.″80	1122	10.11 ± 0.1	15	II	8.69 ± 0.08	0.41 ± 0.02	$0.68^{+0.06}_{-0.16}$	9.08 ± 0.01	$-0.12^{+0.06}_{-0.05}$
NGC4299	$12^{\rm h}21^{\rm m}40^{\rm s}.71$	11°30′06.″12	209	9.06 ± 0.1	8.6	I	9.04 ± 0.02	-0.43 ± 0.02	$-0.72\ ^{+0.53}_{-0.30}$	7.58 ± 0.08	$-0.38^{+0.15}_{-0.15}$
NGC4302	$12^{\rm h}21^{\rm m}42^{\rm s}.24$	14°35′57.″12	1111	10.47 ± 0.1	26	II	9.17 ± 0.07	0.39 ± 0.02	$0.41^{+0.01}_{-0.09}$	9.09 ± 0.01	$0.24^{+0.05}_{-0.02}$
NGC4321[a]	$12^{\rm h}22^{\rm m}54.77^{\rm s}$	15°49′33.″24	1579	10.71 ± 0.1	31	0	9.46 ± 0.02	0.35 ± 0.12	$0.36^{+0.03}_{-0.01}$	9.84 ± 0.00	$-0.16^{+0.17}_{-0.01}$
NGC4330	$12^{\rm h}23^{\rm m}16^{\rm s}.95$	11°22′04.″08	1567	9.63 ± 0.15	18	II	8.65 ± 0.1	0.8 ± 0.04	$0.64^{+0.04}_{-0.02}$	8.34 ± 0.03	$-0.01^{+0.01}_{-0.02}$
NGC4351	$12^{\rm h}24^{\rm m}01^{\rm s}.30$	12°12′15.″12	2388	9.37 ± 0.1	5.1	I	8.48 ± 0.06	0.23 ± 0.02	$0.55^{+0.02}_{-0.13}$	7.85 ± 0.04	$0.14^{+0.10}_{-0.17}$
NGC4380	$12^{\rm h}25^{\rm m}22^{\rm s}.16$	10°01′00.″12	935	10.11 ± 0.1	11	IV	8.1 ± 0.19	1.13 ± 0.2	$1.27^{+0.06}_{-0.16}$	8.59 ± 0.01	$0.37^{+0.06}_{-0.05}$
NGC4383	$12^{\rm h}25^{\rm m}25^{\rm s}.47$	16°28′11.″64	1663	9.44 ± 0.1	6.4	0	9.47 ± 0.05	-0.81 ± 0.2	$-0.39\ ^{+0.01}_{-0.05}$	8.37 ± 0.02	$-0.21^{+0.01}_{-0.17}$
NGC4388	$12^{\rm h}25^{\rm m}46^{\rm s}.61$	12°39′46.″44	2538	10.07 ± 0.1	26	II	8.57 ± 0.26	1.16 ± 0.12	$0.84^{+0.10}_{-0.14}$	8.89 ± 0.01	$0.00^{+0.10}_{-0.02}$
NGC4394	$12^{\rm h}25^{\rm m}55^{\rm s}.66$	18°12′52.″20	772	10.34 ± 0.1	18	IV	8.64 ± 0.03	0.62 ± 0.2	$0.90^{+0.06}_{-0.00}$	7.98 ± 0.04	$1.26^{+0.03}_{-0.02}$
NGC4396	$12^{\rm h}25^{\rm m}59^{\rm s}.66$	15°40′10.″20	−115	9.36 ± 0.1	19	I	8.94 ± 0.08	0.3 ± 0.04	$0.08^{+0.02}_{-0.13}$	8.05 ± 0.04	$-0.10^{+0.13}_{-0.16}$
NGC4402[a]	$12^{\rm h}26^{\rm m}07^{\rm s}.34$	13°06′45.″00	190	10.13 ± 0.1	26	II	8.57 ± 0.18	0.74 ± 0.12	$0.82^{+0.05}_{-0.14}$	9.10 ± 0.01	$-0.10^{+0.04}_{-0.07}$
NGC4405	$12^{\rm h}26^{\rm m}07^{\rm s}.11$	16°10′51.″60	1751	9.75 ± 0.1	8.3	III	7.65 ± 0.26	0.95 ± 0.2	$1.73^{+0.07}_{-0.03}$	8.27 ± 0.02	$0.18^{+0.07}_{-0.00}$
NGC4419	$12^{\rm h}26^{\rm m}56^{\rm s}.35$	15°02′51.″36	−228	10.06 ± 0.1	13	III	7.76 ± 0.63	1.37 ± 0.2	$1.65^{+0.11}_{-0.13}$	9.10 ± 0.00	$-0.23^{+0.09}_{-0.02}$
NGC4424[a]	$12^{\rm h}27^{\rm m}11^{\rm s}.69$	09°25′14.″16	447	9.89 ± 0.1	11	II	8.28 ± 0.07	0.97 ± 0.2	$1.14^{+0.07}_{-0.07}$	8.31 ± 0.01	$0.35^{+0.02}_{-0.06}$
NGC4450	$12^{\rm h}28^{\rm m}29^{\rm s}.23$	17°05′04.″56	2048	10.7 ± 0.1	22	IV	8.45 ± 0.08	1.17 ± 0.2	$1.35^{+0.03}_{-0.00}$	8.67 ± 0.01	$1.00^{+0.16}_{-0.03}$
NGC4457[a]	$12^{\rm h}28^{\rm m}59^{\rm s}.02$	03°34′14.″16	738	10.42 ± 0.1	12	III	8.29 ± 0.11	0.92 ± 0.2	$1.29^{+0.06}_{-0.04}$	9.02 ± 0.01	$0.27^{+0.02}_{-0.03}$
NGC4501	$12^{\rm h}31^{\rm m}59^{\rm s}.33$	14°25′10.″92	2120	11 ± 0.1	35	II	9.22 ± 0.06	0.58 ± 0.12	$0.80^{+0.03}_{-0.02}$	9.69 ± 0.00	$-0.03^{+0.15}_{-0.05}$
NGC4522	$12^{\rm h}33^{\rm m}39^{\rm s}.72$	09°10′26.″76	2332	9.66 ± 0.1	16	II	8.53 ± 0.13	0.86 ± 0.02	$0.79^{+0.04}_{-0.03}$	8.30 ± 0.02	$0.06^{+0.00}_{-0.03}$
NGC4532	$12^{\rm h}34^{\rm m}19^{\rm s}.35$	06°28′05.″52	2154	9.25 ± 0.1	8.0	0	9.29 ± 0.03	-0.06 ± 0.06	$-0.25\ ^{+0.12}_{-0.05}$	8.25 ± 0.02	$-0.58^{+0.15}_{-0.15}$
NGC4533	$12^{\rm h}34^{\rm m}22^{\rm s}.03$	02°19′33.″24	1753	9.2 ± 0.1	9.6	-	8.43 ± 0.11	0.51 ± 0.04	$0.59^{+0.07}_{-0.35}$	6.94 ± 0.26	$0.60^{+0.15}_{-0.15}$
NGC4535[a]	$12^{\rm h}34^{\rm m}20^{\rm s}.26$	08°11′53.″52	1973	10.49 ± 0.1	29	I	9.52 ± 0.02	0.41 ± 0.12	$0.07^{+0.02}_{-0.10}$	9.41 ± 0.01	$-0.06^{+0.08}_{-0.02}$
NGC4536[a]	$12^{\rm h}34^{\rm m}27^{\rm s}.12$	02°11′16.″08	1894	10.19 ± 0.1	42	0	9.68 ± 0.02	0.16 ± 0.12	$-0.26\ ^{+0.02}_{-0.08}$	9.35 ± 0.01	$-0.24^{+0.00}_{-0.09}$
NGC4548[a]	$12^{\rm h}35^{\rm m}26^{\rm s}.64$	14°29′43.″80	498	10.65 ± 0.1	26	IV	8.81 ± 0.03	0.82 ± 0.12	$0.96^{+0.02}_{-0.02}$	8.99 ± 0.01	$0.63^{+0.07}_{-0.09}$
NGC4561	$12^{\rm h}36^{\rm m}08^{\rm s}.14$	19°19′21.″72	1441	9.09 ± 0.1	6.1	0	9.15 ± 0.03	-0.71 ± 0.02	$-0.64\ ^{+0.41}_{-0.46}$	7.31 ± 0.19	$-0.04^{+0.15}_{-0.15}$
NGC4567	$12^{\rm h}36^{\rm m}33^{\rm s}.07$	11°15′29.″16	2213	10.25 ± 0.1	12	0	8.97 ± 0.03	0.13 ± 0.12	$-0.27\ ^{+0.0}_{-0.04}$	8.84 ± 0.00	$0.33^{+0.02}_{-0.02}$
NGC4568	$12^{\rm h}36^{\rm m}34^{\rm s}.34$	11°14′21.″84	2260	10.47 ± 0.1	22	0	9.18 ± 0.05	0.38 ± 0.12	$0.40^{+0.01}_{-0.09}$	9.41 ± 0.00	$-0.08^{+0.05}_{-0.02}$
NGC4569[a]	$12^{\rm h}36^{\rm m}50^{\rm s}.12$	13°09′55.″08	−220	10.86 ± 0.1	50	III	8.79 ± 0.1	1.47 ± 0.2	$1.12^{+0.03}_{-0.04}$	9.58 ± 0.00	$-0.23^{+0.08}_{-0.19}$
NGC4579[a]	$12^{\rm h}37^{\rm m}43^{\rm s}.44$	11°49′05.″52	1627	10.92 ± 0.1	21	IV	8.75 ± 0.12	0.95 ± 0.2	$1.20^{+0.02}_{-0.04}$	9.31 ± 0.00	$0.22^{+0.08}_{-0.17}$
NGC4580	$12^{\rm h}37^{\rm m}48^{\rm s}.38$	05°22′06.″24	1227	9.94 ± 0.1	8.6	III	7.45 ± 0.34	1.53 ± 0.2	$1.99^{+0.11}_{-0.07}$	8.55 ± 0.01	$0.17^{+0.02}_{-0.03}$
NGC4606	$12^{\rm h}40^{\rm m}57^{\rm s}.62$	11°54′43.″56	1653	9.61 ± 0.1	13	III	7.4 ± 0.22	1.64 ± 0.2	$1.86^{+0.01}_{-0.02}$	8.14 ± 0.02	$0.18^{+0.01}_{-0.02}$
NGC4607	$12^{\rm h}41^{\rm m}12^{\rm s}.39$	11°53′09.″60	2284	9.64 ± 0.1	12	III	8.34 ± 0.16	0.82 ± 0.12	$0.96^{+0.02}_{-0.03}$	8.58 ± 0.01	$-0.24^{+0.00}_{-0.03}$

Table 1

(Continued)

Galaxy - (1)	R.A. (J2000) - (2)	Decl. (J2000) - (3)	$v_{\rm opt}$ km s^{-1} (4)	log $M_\star$ $M_\odot$ (5)	$R_\star$ kpc (6)	cl. - (7)	log $M_{\rm H\,I}$ $M_\odot$ (8)	def $_{{\rm H\,I},R_\star}$ dex (9)	def $_{{\rm H\,I},M_\star}$ dex (10)	log $M_{\rm mol}$ $M_\odot$ (11)	def $_{\rm H_2}$ dex (12)
NGC4651	$12^{\rm h}43^{\rm m}42^{\rm s}.72$	$16^\circ23'37''.68$	788	10.31 ± 0.1	13	0	9.61 ± 0.03	-0.3 ± 0.02	$0.09^{+0.03}_{-0.00}$	8.67 ± 0.01	$-0.46^{+0.03}_{-0.01}$
NGC4654[a]	$12^{\rm h}43^{\rm m}56^{\rm s}.76$	$13^\circ07'32''.52$	1035	10.26 ± 0.1	12	II	9.47 ± 0.03	0.12 ± 0.02	$-0.01\ ^{+0.00}_{-0.03}$	9.33 ± 0.00	$-0.15^{+0.03}_{-0.01}$
NGC4689[a]	$12^{\rm h}47^{\rm m}45^{\rm s}.68$	$13^\circ45'42''.12$	1522	10.16 ± 0.1	19	IV	8.67 ± 0.05	0.68 ± 0.12	$0.73^{+0.03}_{-0.11}$	9.02 ± 0.01	$0.04^{+0.01}_{-0.09}$
NGC4694[a]	$12^{\rm h}48^{\rm m}15^{\rm s}.08$	$10^\circ59'00''.60$	1211	9.94 ± 0.1	19	II	8.4 ± 0.03	0.83 ± 0.2	$1.03^{+0.11}_{-0.07}$	8.23 ± 0.02	$0.50^{+0.02}_{-0.03}$
NGC4698	$12^{\rm h}48^{\rm m}22^{\rm s}.99$	$08^\circ29'15''.00$	1032	10.49 ± 0.1	19	I	9.21 ± 0.03	0.02 ± 0.2	$0.37^{+0.02}_{-0.10}$	7.94 ± 0.10	$1.40^{+0.08}_{-0.02}$
NGC4713	$12^{\rm h}49^{\rm m}57^{\rm s}.65$	$05^\circ18'39''.60$	631	9.31 ± 0.16	10	0	9.46 ± 0.03	-0.31 ± 0.04	$-0.42\ ^{+0.10}_{-0.00}$	8.38 ± 0.02	$-0.56^{+0.22}_{-0.24}$
NGC4772	$12^{\rm h}53^{\rm m}29^{\rm s}.12$	$02^\circ10'06''.24$	1042	10.18 ± 0.1	9.9	0	8.92 ± 0.06	0.15 ± 0.2	$0.48^{+0.02}_{-0.09}$	7.40 ± 0.27	$1.70^{+0.00}_{-0.10}$
NGC4808	$12^{\rm h}55^{\rm m}48^{\rm s}.94$	$04^\circ18'15''.12$	738	9.63 ± 0.1	11	0	9.55 ± 0.03	-0.58 ± 0.04	$-0.27\ ^{+0.01}_{-0.03}$	8.74 ± 0.01	$-0.41^{+0.00}_{-0.03}$
VCC1581	$12^{\rm h}34^{\rm m}45^{\rm s}.30$	$06^\circ18'02''.00$	2039	8.47 ± 0.1	-	-	8.5 ± 0.04	-0.06 ± 0.06	$-2.63\ ^{+0.14}_{-0.14}$	$\leqslant 6.84$	$\geqslant 0.69$

Notes. Columns are (1) common name; (2) R.A. (J2000) of the galaxy optical center; (3) decl. (J2000) of the galaxy optical center; (4) optical heliocentric recession velocity; (5) stellar mass (see Section 3.2.1); (6) optical radius, defined as the isodensity radius of the stellar mass distribution, where $\Sigma_\star = 1\ M_\odot {\rm pc}^{-2}$ (Section 3.2.1). The uncertainty is dominated by the resolution of the stellar mass surface-density maps, and therefore equals 0.3 kpc for all galaxies; (7) H I classification from VIVA (see Section 3.6); (8) H I mass, from Table 3 in Chung et al. (2009); (9) H I deficiency, from Table 3 in Chung et al. (2009, see also Section 3.1); (10) H I deficiency, calculated using the predicted H I mass from field galaxies at fixed stellar mass (see Section 3.1); (11) molecular gas mass, from Table 2 in B21; (12) molecular gas deficiency, see Section 3.2. Columns 2–4 are drawn from the NASA/IPAC Extragalactic Database (NASA/IPAC Extragalactic Database (NED), 2019).

[a] The ALMA observations of these galaxies are from the archive; see Section 2 for more details.

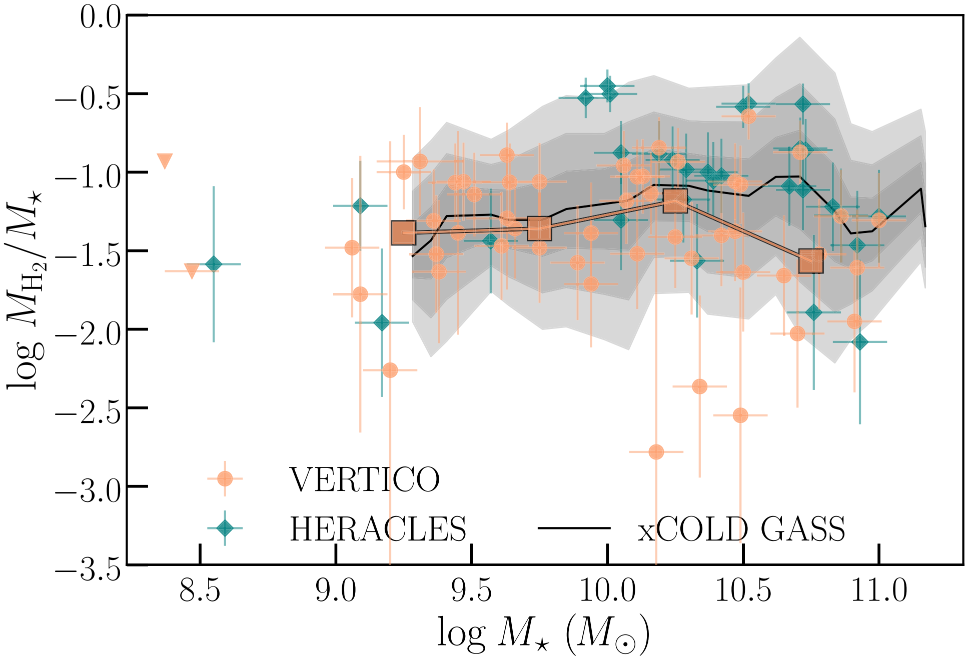

Figure 1. H_2 fractions of VERTICO (orange dots) and HERACLES (teal diamonds) galaxies compared to 303 galaxies from xCOLD GASS, as a function of stellar mass. Downward triangles represent upper limits. The solid black line represents the rolling median of the xCOLD GASS sample, while the shaded gray areas indicate the 1, 2, and 3σ spread (from dark to light, respectively). The connected orange squares with black edges are the median H_2 fractions of VERTICO galaxies in four equal stellar mass bins in log space (excluding the two upper limits). VERTICO galaxies with log $M_\star \gtrsim 9.75$ log $M_\odot$ are moderately but systematically H_2 deficient, while low-mass VERTICO galaxies have H_2 fractions similar to or higher than xCOLD GASS galaxies at fixed $M_\star$. HERACLES galaxies are relatively H_2 rich.

appropriate version. For the imaging of both the ACA and the TP data the PHANGS-ALMA Imaging Pipeline Version 1.0 and the PHANGS-ALMA TP Pipeline were used, respectively (Herrera et al. 2020; Leroy et al. 2021b). Three modifications were implemented in the Imaging Pipeline to optimize for the VERTICO sample, which are described in detail in Section 3.1 of B21. A Briggs weighting scheme was adopted (Briggs 1995), with a robust parameter of 0.5. The total power data were processed at their native velocity resolution of ∼3 km s^{-1}, and no other modifications were made to the TP Pipeline. For the PHANGS-VERTICO galaxies, calibrated TP cubes were kindly provided to us by Adam Leroy on behalf of the PHANGS-ALMA team in private communication. Finally, the total power data were combined with the ACA data via feathering using the PHANGS-ALMA pipeline (Leroy et al. 2021b).

The median spatial resolution of the resulting data cubes is ∼8″ (∼640 pc at the distance of Virgo), and the final velocity resolution is 10 km s^{-1}. The flux calibration uncertainty is typically 5%–10%.[19] The typical root-mean-square (rms) sensitivity reached with the ACA, after an average integration time of 3.7 hours on source, is 10.6 mJy $beam^{-1}$ per 10 kms channel. All galaxies were detected in CO except IC3418 and VCC1581, for which we calculated 3σ upper limits. Although the presence of H I emission in IC3418 was confirmed later by Kenney et al. (2014), its image is not available (unlike VCC1581) and it is not considered in this work beyond Figure 1.

2.1. Control Samples

We use two types of comparison samples. First, the extended Galaxy Evolution Explorer (GALEX) Arecibo SDSS Survey (xGASS; Catinella et al. 2018) and the extended CO Legacy Database for GALEX Arecibo SDSS Survey (xCOLD GASS; Saintonge et al. 2017) are used to compare global H I and H_2 masses in VERTICO to those of the general population of galaxies at fixed stellar mass, and estimate H I and H_2 deficiencies. After applying a small number of selection criteria (described below), these samples comprise several hundreds of galaxies, thus providing a good representation of the galaxy population throughout the relevant stellar mass range. Second, for a comparison of *resolved* properties of VERTICO galaxies with control galaxies, we use the HEterodyne Receiver Array CO-Line Extragalactic Survey (HERACLES, Leroy et al. 2009). This sample is described in detail in Section 2.1.2.

In Figure A1, all three control samples, as well as the VERTICO sample, are shown on the SFR–$M_\star$ plane. Stellar masses and star-formation rates for x(COLD) GASS were taken from GALEX-SDSS-WISE Legacy Catalog (GSWLC, Salim et al. 2016), as these are consistent with those from the $z = 0$ Multiwavelength Galaxy Synthesis (z0MGS, Leroy et al. 2019), which are adopted for the VERTICO sample (see Section 3.2.1). Galaxies for which no 22 μm detection is available (used for deriving SFRs) have upper limits on their SFRs are indicated with down-pointing triangles. VERTICO galaxies occupy a similar region in this plane as star-forming (i.e., non-quiescent) x(COLD) GASS galaxies. HERACLES galaxies have enhanced SFRs at fixed stellar mass, which is likely due to selection effects (Section 2.1.2) This implies that HERACLES galaxies may not be typical field galaxies, and may have increased gas fractions, if they follow the Kennicutt-Schmidt relation (Schmidt 1959; Kennicutt 1998). We should keep this in mind when we compare results from the VERTICO sample to those from the HERACLES sample.

2.1.1. xGASS & xCOLD GASS

As described in Section 2, the VERTICO sample consists exclusively of late-type galaxies. In the field, such galaxies are

---

[19] See the ALMA Technical Handbook: https://almascience.nrao.edu/documents-and-tools/cycle8/alma-technical-handbook.

expected to lie on, or close to, the star-formation main sequence (SFMS). Therefore, to ensure a fair comparison with VERTICO, we only consider galaxies from xGASS and xCOLD GASS within 2σ from the SFMS (Elbaz et al. 2007). Furthermore, galaxies with confused H I emission (i.e., the H I emission from multiple sources cannot be separated reliably), as identified by Catinella et al. (2018), are eliminated from the xGASS sample. After applying these selection criteria, the comparison sample from xGASS consists of 541 galaxies with detected H I, and 33 with upper limits.

Molecular gas masses from xCOLD GASS were corrected for the difference in α_{CO} (see Section 3.2; xCOLD GASS uses the metallicity-dependent α_{CO} from Accurso et al. 2017). The final comparison sample consists of 303 galaxies, 44 of which are upper limits.

Upper limits are taken into account in the calculation of the median H_2 mass using survival analysis (a statistical method designed to take into account "censored" data: measurements for which only an upper or lower limit is available). We used the Kaplan–Meier estimator, implemented in the `Python` package `Lifelines` (Davidson-Pilon 2019), to estimate the true cumulative distribution of H_2 mass with upper limits taken into account. The median H_2 mass was estimated from the resulting distribution. The Kaplan–Meier estimator takes censored data into account assuming they follow a similar distribution to the measured data. Finally, we calculate the rolling median of the H_2 mass by dividing the sample into 10 stellar mass bins and using a shift of half a bin.

2.1.2. HERACLES: A Resolved Control Sample

We compare the resolved properties of VERTICO galaxies to those from HERACLES. We first remove galaxies that are also in VERTICO from the HERACLES sample (NGC4254, NGC4321, NGC4536, NGC4569, and NGC4579), as well as interacting galaxies (NGC2146, NGC2798, NGC3034, NGC3077, and NGC5713), except for those with a significantly less massive or gas-poor companion, such as NGC5194 (M51). The remaining sample consists of 21 galaxies detected in CO. Resolved quantities are calculated from the HERACLES moment 0 maps at native resolution (the typical beam size is $b_{maj} \sim 13''$), in the same way as those of VERTICO. These maps are calculated from the 10 km s^{-1} cubes, using the VERTICO data products pipeline (B21, Section 4.1). NGC4214, NGC2841, and NGC4725 are omitted from the H_2 surface-density analysis due to their high inclination (see Section 3.5).

Global molecular gas mass fractions of the HERACLES sample are shown in Figure 1. Here we can see that HERACLES galaxies are relatively gas rich. The HERACLES sample was based on The H I Nearby Galaxy Survey (THINGS, Walter et al. 2008), which was in turn based on the Space Infrared Telescope Facility (SIRTF) Nearby Galaxies Survey (SINGS, Kennicutt et al. 2003). By design, this sample has a flat far-infrared (FIR) luminosity distribution (as measured at 60 μm with the Infrared Astrononomical Satellite, IRAS). This means that, compared to the actual FIR luminosity distribution of galaxies in the local universe, FIR-faint galaxies are significantly under-represented (see also Figure 6 in Kennicutt et al. 2003). Therefore, it is likely that the SINGS, THINGS, and HERACLES samples are biased toward galaxies with high (atomic and molecular) gas masses (e.g., Saintonge et al. 2018). This should be kept in mind throughout the remainder of this work.

3. Methods

3.1. HI Deficiency

For the majority of this work, H I deficiencies are adopted from Chung et al. (2009), who use the Hubble-type independent definition from Haynes & Giovanelli (1984):

$$\mathrm{def}_{\mathrm{HI},R_\star} = \langle \log \bar{\Sigma}_{\mathrm{HI}} \rangle - \log \bar{\Sigma}_{\mathrm{HI}}, \tag{1}$$

where $\bar{\Sigma}_{\mathrm{HI}} \equiv S_{\mathrm{HI}} / D_{\mathrm{opt}}^2$, where S_{HI} is the H I flux in Jy km s $^{-1}$ and D_{opt} is the diameter of the optical disk in arcminutes. $\bar{\Sigma}_{\mathrm{HI}}$ is the mean H I surface density within the optical disk, and $\langle \log \bar{\Sigma}_{\mathrm{HI}} \rangle = 0.37$ for all Hubble types. Uncertainties on the H I deficiency reflect the difference with the Hubble-type dependent deficiency for the same object (in reality $\langle \log \bar{\Sigma}_{\mathrm{HI}} \rangle$ varies somewhat with Hubble type, see Section 5.5 in Chung et al. (2009) for more details). A common distance of 16 Mpc was adopted to calculate these deficiencies in Chung et al. (2009), sufficiently similar to the distance of 16.5 Mpc adopted in this work for any differences in H I measurements to be negligible.

Since such a well-defined mass–size relationship does not exist for CO, the expected molecular gas mass in the equation for gas deficiency (Equation (3)) is derived from the median molecular gas mass of control galaxies at fixed stellar mass, rather than the optical size of the host galaxy (see Section 3.2). To ensure a fair comparison between deficiencies in both gas phases, we consider a second definition of H I deficiency, similar to that for H_2 deficiency:

$$\mathrm{def}_{\mathrm{H\,I},M_\star} = \log M_{\mathrm{H\,I,exp}} - \log M_{\mathrm{H\,I,meas}}, \tag{2}$$

where the expected H I mass, $M_{\mathrm{H\,I,exp}}$, is the median H I mass at fixed stellar mass from a control sample from xGASS (see 2.1.1), and $M_{\mathrm{H\,I,meas}}$ is the measured H I mass.

Uncertainties in def $_{\mathrm{H\,I},M_\star}$ are calculated by combining the uncertainty in the H I mass and that resulting from the uncertainty in the stellar mass. The 1σ spread in H I mass fractions in the control sample is $\sim$0.7 dex and varies somewhat with stellar mass. This spread is not taken into account in the uncertainty in $\mathrm{def}_{\mathrm{H\,I},M_\star}$. The resulting H I deficiencies are listed in Table 1.

3.2. H_2 Deficiency

The mass–size relation for H_2 has not been defined as well as for H I (see e.g., B21). Additionally, the scatter in the relationship between stellar mass and molecular gas mass is smaller than that in the relationship between optical size and molecular gas mass (Boselli et al. 2014a). Therefore, we use the median H_2 mass of a control sample at fixed stellar mass to estimate the expected H_2 mass. Then the H_2 deficiency can be defined as follows:

$$\mathrm{def}_{\mathrm{H}_2} = \log M_{\mathrm{H}_2,\mathrm{exp}} - \log M_{\mathrm{H}_2,\mathrm{meas}}, \tag{3}$$

where $M_{\mathrm{H}_2,\mathrm{exp}}$ corresponds to the expected molecular gas mass of a galaxy and $M_{\mathrm{H}_2,\mathrm{meas}}$ is its measured global molecular gas mass. The control sample we use to calculate $M_{\mathrm{H}_2,\mathrm{exp}}$ is xCOLD GASS (see Section 2.1.1).

Global molecular gas mass estimates for the VERTICO sample are described in detail in Section 4.4 of B21, and are summarized here. Molecular gas masses are derived from CO luminosities as follows:

$$M_{\rm mol} = \frac{\alpha_{\rm CO}}{R_{21}} L_{\rm CO}, \quad (4)$$

where $\alpha_{\rm CO}$=4.35 M $_\odot$ pc^{-2} (K km s^{-1})$^{-1}$, corresponding to the Galactic value of $X_{\rm CO} = 2 \times 10^{20}$ cm^{-2} (K km s^{-1})$^{-1}$ recommended by Bolatto et al. (2013), and $R_{21} \equiv$ CO(2 − 1)/CO(1 − 0) = 0.8 as found by e.g., Leroy et al. (2009) and B21. The CO line luminosities are calculated following Solomon & Vanden Bout (2005):

$$L_{\rm CO} = 3.25 \times 10^7 \, S_{\rm CO} \, \nu_{\rm obs}^{-2} \, D_L^2 \quad (5)$$

where $S_{\rm CO}$ is the integrated CO line flux in Jy km s^{-1}, $\nu_{\rm obs}$ the observed frequency in GHz, and D_L the luminosity distance to the source in Mpc.

Note that the adopted $\alpha_{\rm CO}$ includes a 36% contribution from helium. Therefore, the masses calculated here are total molecular gas masses.

Uncertainties in H_2 deficiency are calculated by combining the uncertainty in the H_2 mass and that resulting from the uncertainty in the stellar mass. The 1σ spread in molecular gas fractions in the control sample is ∼0.4 dex and varies somewhat with stellar mass (see Figure 1). This spread is not taken into account in the uncertainty in def$_{\rm H_2}$. Molecular gas mass deficiencies are listed in Table 1.

Molecular gas fractions in the VERTICO sample are shown in Figure 1 as orange dots, overlaid on the sample from xCOLD GASS (see Section 2.1.1), whose median is shown as a solid black line, while the 1, 2, and 3σ spread is shown as shaded gray areas. The medians of the VERTICO sample, in stellar mass bins of 0.5 dex, are shown as orange squares. H_2 fractions of the HERACLES sample are shown as teal diamond markers. VERTICO galaxies with stellar masses log $M_\star/M_\odot \gtrsim 9.75$ are marginally but systematically H_2 deficient, with the median molecular gas fractions of the stellar mass bins lying 0.1–0.5 dex below the xCOLD GASS rolling median. VERTICO galaxies with stellar masses log $M_\star/M_\odot \lesssim 9.75$ have H_2 fractions similar to, or marginally higher than, those of xCOLD GASS galaxies at fixed stellar mass. HERACLES galaxies are H_2-rich compared to xCOLD GASS at fixed stellar mass (see also Section 2.1.2).

There is a subsample of VERTICO galaxies that overlaps with a subsample of the Herschel Reference Survey (HRS, Boselli et al. 2010) for which high-quality CO data are available (Kuno et al. 2007). H_2 deficiencies for these galaxies were estimated by Boselli et al. (2014a) similarly to this work, but where $M_{\rm H_2,exp}$ in Equation (3) is defined as follows:

$$\log M({\rm H_2}) = c \times \log({\rm Variable}) + d, \quad (6)$$

where the coefficients c and d are derived from linear fits to the relationship between log M(H$_2$) and Variable, where the latter is chosen to be $M_\star$. The sample used to derive this linear fit consists of all HRS galaxies with H I deficiencies ⩽ 0.4, and upper limits are treated as measurements. An extensive description of the calibration of this H_2 deficiency parameter can be found in Section 4.1 in Boselli et al. (2014a).

A comparison between H_2 deficiencies from that work and those derived here is shown in Figure A2(b). H_2 deficiencies of the VERTICO sample calculated using Equation (3) are systematically lower than those of the HRS sample by ∼0.25 dex, and by ∼0.5 dex in case of the two galaxies with the largest H_2 deficiencies. There is a systematic offset in molecular gas masses in VERTICO and published molecular gas masses for the same objects in Boselli et al. (2014a), which is the result of differences in the calibration approach (see Section 4.3 in B21). This likely causes differences in the derived H_2 deficiencies. Moreover, the control samples used to calibrate the relation are significantly different. Boselli et al. (2014a) calibrate the relation against a subsample of the HRS consisting of 101 spiral galaxies for which CO data are available, and which have H I deficiencies ⩽ 0.4 dex. This method could introduce a bias toward gas-rich galaxies, which would result in an overestimation of H_2 deficiencies for the Virgo systems. Since our def $_{{\rm H\,I},M_\star}$ parameter agrees well with the def $_{{\rm H\,I},R_\star}$ parameter from Chung et al. (2009, see also Figure A2a), and H_2 deficiency was derived similarly, we are confident that the H_2 deficiencies we derive are suitable for the purpose of this work.

3.2.1. Stellar Masses and Radii

Stellar masses for the VERTICO sample are adopted from the $z = 0$ Multiwavelength Galaxy Synthesis (z0MGS, Leroy et al. 2019), who use the initial mass function (IMF) from Kroupa & Weidner (2003). The only exception is IC3418, which is not included in z0MGS. For this galaxy, we adopt a stellar mass of $M_\star = 10^{8.37} M_\odot$, following Fumagalli et al. (2011 see also Section 2.2 in B21). Stellar radii are here defined as the isodensity radius with a threshold of $\Sigma_\star = 1\ M_\odot$pc^{-2}. These radii are measured by identifying the outermost annulus or slice of the stellar mass radial profile (measured as described in Section 3.3) that is still above this threshold, and adopting its radius. For consistency with the gas radius and surface-density measurements (see Section 3.3) the stellar surface-density maps are not corrected for inclination before radial profiles are derived. The uncertainty in the radius is a combination of the resolution of the stellar mass surface-density maps (9 ″, corresponding to ∼720 pc at the distance of the Virgo cluster) and the uncertainty in the stellar mass surface density.

We produce stellar mass surface-density maps from Wide-field Infrared Survey Explorer (WISE) band 1 photometry, following the procedure laid out in Leroy et al. (2019 and therefore using the same IMF as that used for the stellar masses, see above). All images are convolved from their native resolution to a 9″ Gaussian beam, using the convolution kernels from Aniano et al. 2011. All Gaia DR2 stars within the image area are masked. Image backgrounds are estimated and subtracted with the `Background2D` function from `Astropy`. For each pixel, we determine the local mass-to-light ratio (at 3.4 μm) using the WISE band 3 to WISE band 1 color as an "sSFR-like" proxy, and following the calibrations given in the Appendix of Leroy et al. (2019). The WISE band 1 images are then combined with the derived mass-to-light ratios to produce resolved stellar mass surface-density maps in units of $M_\odot$ pc^{-2}.

3.3. Radial Profiles

H_2 radial profiles are calculated as described in Section 4.3 of B21. In summary, they reflect the azimuthally averaged integrated H_2 surface densities in elliptical annuli overlaid on the moment 0 maps at native resolution (these maps can be seen in Appendix A of B21). While some authors opt to correct for inclination in order to obtain a measure of the intrinsic surface density (assuming the gas is distributed in a flat disk), here we do not apply this correction, due to the disturbed nature of several of the sources. Similarly, it should be kept in mind that any extraplanar gas that may be present in these disturbed sources could be assigned to artificially large radii due to projection effects, especially in highly inclined galaxies. This would result in a flattened radial profile, and possibly an overestimation of the radius of the molecular gas "disk."

Pixels that do not contain any detected emission are included as zeros. This means that the surface density at each radius represents the average surface density in the *entire* corresponding annulus, rather than the average surface density of the molecular gas detected inside the annulus. Therefore, on the outskirts of the molecular gas disks, where CO is not detected in all pixels, this can result in low average molecular gas surface densities. This effect will be stronger in galaxies with very asymmetric molecular gas disks. We continue to add annuli until there are no more detected pixels in the outer annulus. Since we are working with clipped moment 0 maps, all non-zero pixels in the map are significant.

To allow for accurate interpolation in our calculation of the radial profiles, we use annuli with widths of one pixel ($2''$, equivalent to ∼160 pc at the distance of Virgo) across the minor axis. This approach differs from that of B21, who use annuli with widths of one beam ($7''$–$10''$; B21, Table 2) across the minor axis. To allow for a fair comparison between galaxies, we then interpolate the resulting radii (R) to match certain fractions of the galaxy's stellar radius (at each $\Delta 0.2 R_\star$). This means that in some cases ΔR can be smaller than one beam, in which case the integrated H_2 surface densities in the corresponding annuli are not independent. Since we are interested in the relative shapes of the profiles, and their corresponding radii and average surface densities, this will not impact our analysis.

The eccentricities of the annuli, along with the inclinations and position angles of the galaxies, are listed in Table 1 of B21. For highly inclined ($i \gtrsim 80^o$) galaxies we take slices along the major axis instead of annuli (extending infinitely in the direction of the minor axis). The emission in the corresponding slices on each side of the galactic center (at the same galactocentric radius) is then averaged to obtain the radial profile (see also B21).

Molecular gas radial profiles of all CO-detected VERTICO galaxies are shown in B21; Figure 9, and in Figure A3 along with their H I radial profiles (which were calculated in the same way, i.e., by placing annuli on the observed (inclination-uncorrected) H I surface-density maps), as well as the ratio between both profiles. For this figure, the $15''$ resolution VERTICO moment 0 maps were used, to match the H I data.

3.4. H_2 Radii

In this paper, the radius of the H_2 disk is defined as its isodensity radius: the radius at which the observed surface density of the molecular gas disk drops below a certain threshold value (henceforth referred to as the "isodensity threshold"). In cases where the surface density is not described by a strictly declining function (for example when a galaxy has pronounced spiral arms and inter-arm regions with low molecular gas surface densities), it is possible that this threshold is reached at multiple radii. In such cases, the outermost radius is defined to be the isodensity radius.

Typically, the radius of the H_2 disk is defined at isodensity thresholds of $\sim 5\, M_\odot \mathrm{pc}^{-2}$, where the molecular gas starts dominating the cold gas reservoir (e.g., Walter et al. 2008; Leroy et al. 2008). However, depending on which part of the disk we are interested in (e.g., the core or the very outskirts), it is sometimes useful to use lower or higher isodensity thresholds. Throughout this work, we specify which isodensity threshold is used to define the radius of the molecular gas disk for a particular investigation (e.g., in Figure 4).

Because the main goal of this work is to compare different galaxies, and because we are interested in the *relative* size of the molecular gas disk, H_2 radii are normalized by the radius of the stellar disk (see Section 3.2.1).

3.5. Median H_2 Surface Densities

The median H_2 surface density is here defined as the median H_2 surface density of the moment 0 map within an elliptical aperture of which the semimajor axis is a certain observed fraction of $R_\star$. For highly inclined galaxies and galaxies with very little flocculent CO emission, such a median surface density is not well defined. For this reason, we do not measure it for the following galaxies: NGC4192, NGC4216, NGC4222, NGC4299, NGC4302, NGC4330, NGC4388, NGC4396, NGC4402, NGC4533, NGC4607, NGC4698, and NGC4772. As a result, median H_2 surface densities are measured for 34/49 detected VERTICO galaxies. Median H_2 surface densities will be studied as a function of H I and H_2 deficiency (see Section 4.4 and Figure 5).

3.6. Classification of HI Removal Stages

Yoon et al. (2017) study in detail the H I properties of the galaxies in VIVA, the sample on which the VERTICO sample is based. They are particularly interested in H I deficiency, radius, and morphology, since any gas stripping is most notably reflected in these parameters. Therefore, to study the effects of gas stripping as systematically as possible, they define a classification for the Virgo galaxies based on the combination these H I properties. In particular, each class spans a limited range of H I deficiency and relative H I extent. This classification is described in detail in Section 2.1 of Yoon et al. (2017). In summary, galaxies comprising each class are:

1. Galaxies with a one-sided H I feature, no truncation of the disk and a relatively symmetric stellar disk. Their H I deficiency varies but is overall close to that in field galaxies.
2. Galaxies with highly asymmetric H I disks, caused by tails and/or asymmetric truncation, deficient in H I (average deficiency (def $_{\mathrm{H\,I},R_\star}$) of ∼0.8 dex).
3. Galaxies with symmetric but severely truncated H I disks that are extremely H I deficient (average deficiency of $\gtrsim$ 1.4 dex).
4. Galaxies with symmetric H I disks that are only marginally truncated, but with lower H I surface density than the other classes, and an average deficiency of ∼0.8 dex (similar to class II).
5. Galaxies that do not fit in the above classes, including galaxies that resemble "normal" field spirals, extremely H I-rich galaxies with extended H I disks, galaxies that have asymmetric H I disks but no truncation, showing clear signs of tidal interaction.

To build upon this work by Yoon et al. (2017), and investigate if there is any correlation between their H I classification and

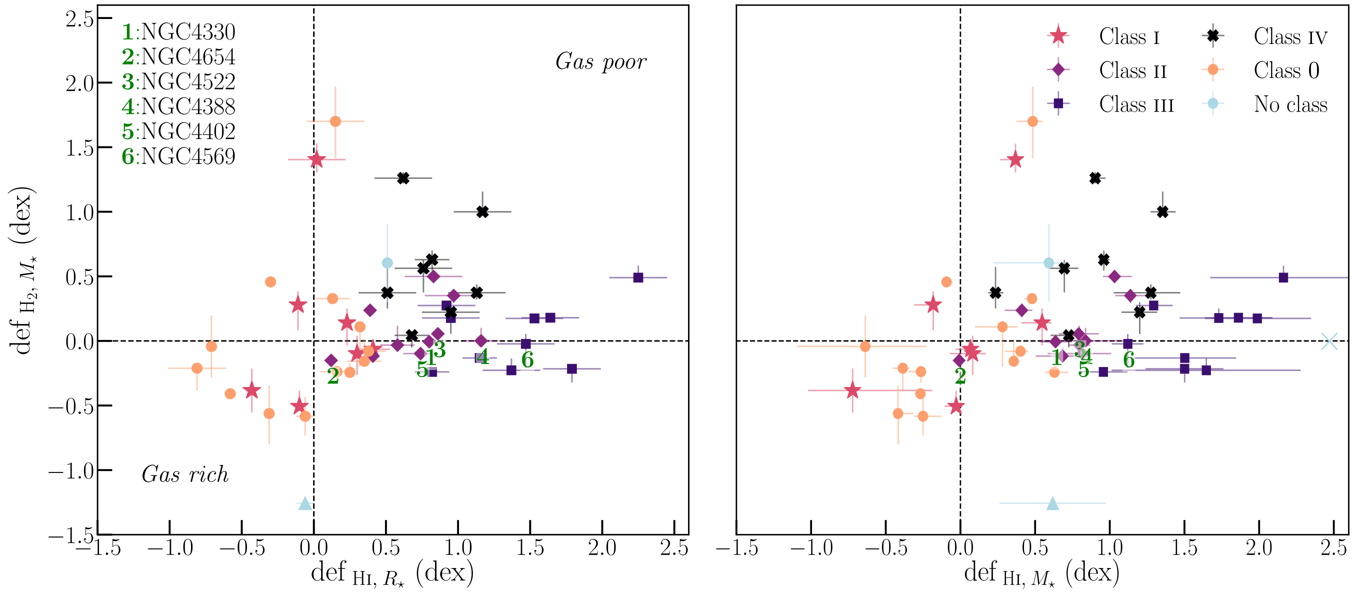

Figure 2. H_2 deficiency as a function of H I deficiency, where H I deficiency is estimated in two different ways (def $_{\rm H\,I, R_\star}$, left-hand panel, and def $_{\rm H\,I, M_\star}$, right-hand panel). Classes refer to the H I classification from Yoon et al. (2017, see Section 3.6), based on deficiency and morphology. VCC1581, which was not detected in CO, is represented by the light-blue triangle, indicating the lower limit on its molecular gas deficiency. The x-shaped marker in the right panel indicates IC3418, which is a lower limit both in H I and H_2 deficiency (it is not present in the left-hand panel because no limit on the H I deficiency was provided by Chung et al. 2009). The numbered galaxies (green numbers are placed below the relevant markers) represent well-studied "smoking-gun" RPS galaxies, listed in the top-left corner in order of pre-to-post RP peak. There is a weak correlation between H I and H_2 deficiency: the Spearman correlation coefficient is 0.28 ± 0.05, with a typical p value of 0.05, for the left-hand panel and 0.36 ± 0.04, with a typical p value of 0.01, for the right-hand panel. Most galaxies lie in the upper-right quadrant, and are thus both H I and H_2 deficient. On average, galaxies that have H I reservoirs similar to those of field galaxies (class 0 galaxies) are least H_2 deficient, while galaxies that are H I deficient because of their lower H I surface densities (class IV galaxies) are most H_2 deficient. VERTICO galaxies undergoing RPS are relatively H_2-rich compared to other VERTICO galaxies with similar H I deficiencies.

molecular gas deficiency, these classes are highlighted in Figure 2. Note that the dwarf galaxy NGC4533 is the only galaxy in the VERTICO sample for which no H I class is given in Yoon et al. (2017), who exclude 5 dwarf galaxies from the classification scheme. The reason for this is that such dwarf galaxies might be more sensitive to their local environment rather than their orbital history, which was the main focus of the VIVA classification.

4. Results

4.1. Do HI Deficiencies Predict H_2 Deficiencies?

Figure 2 shows the relationship between H I deficiency and H_2 deficiency. The relationship is shown for two different definitions of H I deficiency: def $_{\rm H\,I, R_\star}$ in the left-hand panel, and def $_{\rm H\,I, M_\star}$ in the right-hand panel (see Section 3.1 for their respective definitions). H I deficiencies from both definitions correlate well (the typical scatter is ~0.2 dex, see Figure A2(a)). The classes in the legend refer to the H I classification described in Section 3.6. Six well-studied cases of galaxies undergoing RPS are highlighted with red numbers 1–6, and listed in the top-left corner of the left-hand panel in order of pre-to-post RP peak (Vollmer 2003, 2009; Vollmer et al. 2004, 2008, 2012; Boselli et al. 2006, 2016; Lee et al. 2017; Lee & Chung 2018).

There is a weak correlation between H I and H_2 deficiency. The Spearman correlation coefficient is 0.28 ± 0.05 in the left-hand panel (where def $_{\rm H\,I} \equiv$ def $_{\rm H\,I, R_\star}$), with a typical p value of 0.05, and 0.36 ± 0.04 in the right-hand panel (where def $_{\rm H\,I} \equiv$ def $_{\rm H\,I, M_\star}$), with a typical p value of 0.01. Uncertainties on the Spearman correlation coefficient were obtained using a Monte Carlo analysis, and represent the spread in the values of Spearman's correlation coefficient after calculating it 1×10^5 times, perturbing each point by its error bar. The weak correlation between H I and H_2 deficiency suggests that the environmental effects removing H I from galaxies also affect the molecular gas, albeit to a lesser extent.

Most galaxies are located in the upper-right quadrant of Figure 2, meaning they are both H I and H_2 deficient. This suggests that, despite the lack of a stronger correlation between their deficiencies, both the atomic and molecular gas phases are affected by environmental processes.

In terms of H I classes, there is a significant scatter in H_2 deficiency within each class. There are, however, some differences between the classes. Except for a few outliers, class 0 galaxies (galaxies with "normal" H I reservoirs that resemble those of field galaxies) have normal to high H_2 fractions, in line with their morphologically normal, non-deficient H I reservoirs. Class I galaxies, which exhibit one-sided H I features but otherwise have H I and stellar disks similar to those of field galaxies, are H_2 normal. Classes II and III (galaxies with moderate to extreme asymmetries and significant H I deficiencies) have moderately deficient H_2 reservoirs. Galaxies that are H I deficient due to their lower H I surface densities (class IV galaxies) have relatively high H_2 deficiencies. The six known RPS galaxies are relatively H_2 rich compared to other VERTICO galaxies with similar H I deficiencies.

4.2. H_2 Radial Profiles by HI Deficiency

Median $\Sigma_{\rm H_2}$ radial profiles are shown in Figure 3, they are divided into three equal bins of def $_{\rm H\,I,\,R_\star}$, indicated by the color bar. In the color bar, the white dots show the distribution of H I

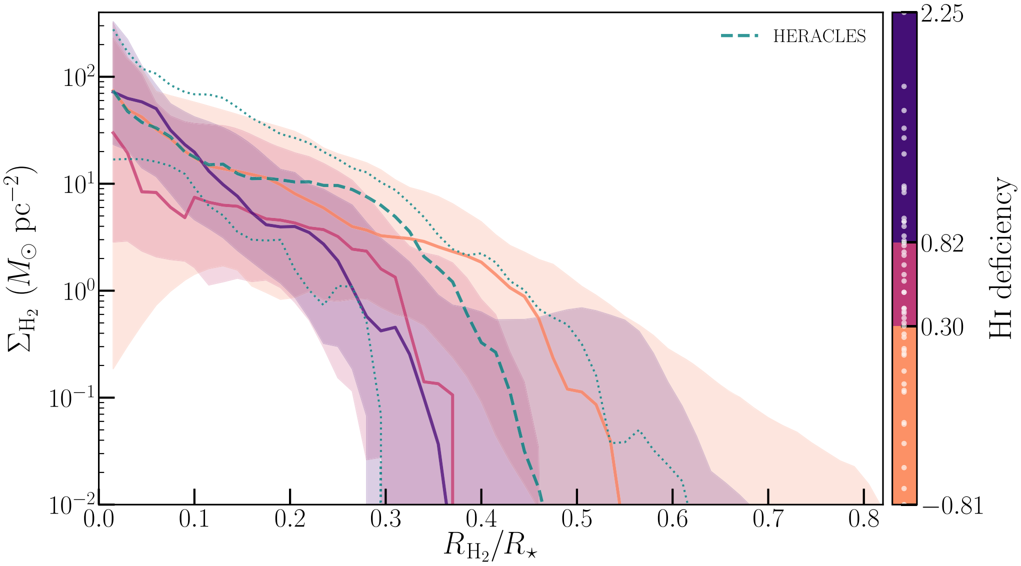

Figure 3. Observed median H_2 radial profiles of VERTICO galaxies shown in three bins of ~15 galaxies, sorted by H I deficiency. The shaded areas highlight the 16th to 84th percentile regions. The teal dashed line represents the median profile of 21 HERACLES field galaxies. Its 16th to 84th percentiles are indicated with dotted lines. The distribution of the H I deficiencies in the sample is shown on the color bar using white dots. More H I-deficient galaxies have steeper and more truncated H_2 radial profiles. The median radial profile of HERACLES galaxies lies between those of the most H I-rich and moderately H I-deficient VERTICO galaxies.

deficiencies. The solid lines show the medians of the radial profiles in each bin; the shaded areas cover the 16th to 84th percentile regions. The teal dashed line represents the median H_2 radial profile of the 21 galaxies in the HERACLES field sample, whose 16th to 84th percentiles are indicated with dotted lines. The x-axis is normalized by the isodensity radius of the stellar disk (at $\Sigma_\star(R_\star) = 1 M_\odot$ pc^{-2}), the y-axis is not normalized.

More strongly H I-deficient galaxies have steeper and more truncated H_2 radial profiles. This suggests that the environmental processes acting on the atomic gas cause outside-in removal of the molecular gas. The median H_2 radial profile of the HERACLES sample lies between those of the most H I-rich and moderately H I-deficient VERTICO galaxies.

4.3. H_2 Radii

Figure 4 shows the H_2 disk radii (R_{H_2}) as a function of H I deficiency (left panel) and H_2 deficiency (right panel), for a Σ_{H_2} threshold 1 $M_\odot$pc^{-2}. As can be seen in Figure 3, this threshold probes the low-density gas at the outskirts of the H_2 disk, which is the gas most likely to be affected by environmental mechanisms. R_{H_2} declines significantly with H I deficiency; the Spearman correlation coefficient is $r_S = -0.44 \pm 0.07$, with a typical p value of 1.7×10^{-3}. Outliers of this correlation are NGC4561, NGC4654, NGC4419, and NGC4380 (annotated in the figure). NGC4561 only has a few "blobs" of detected molecular gas, which means that it does not have a well-defined H_2 radius. NGC4380 has a large, regular-looking molecular gas disk. NGC4654 also has a large molecular gas disk, with a one-sided RPS feature. Although NGC4419 is not among the "well-studied" RPS cases, the morphology of its molecular gas disk suggests that it is likely also undergoing RPS (see Appendix A in B21).

There is a weaker anticorrelation between H_2 radius and H_2 deficiency, which is likely intrinsic. The Spearman correlation coefficient of this relation is $r_S = -0.29 \pm 0.05$, with a typical p value of 0.04. Outliers of this relation are NGC4772, NGC4698, NGC4450, and NGC4394. Like NGC4561, NGC4772 only has very little, patchy, detected molecular gas, which results in a large radius for its strong H_2 deficiency. In NGC4698, the molecular gas is distributed in a ring, resulting in a similar effect. NGC4450 has a one-sided molecular gas feature, which is responsible for its relatively large H_2 radius. The molecular gas in NGC4394 is also patchy, again resulting in a strong deficiency compared to its H_2 radius.

The anticorrelation between H I deficiency and R_{H_2} suggests that the environmental mechanism(s) removing H I from galaxies also cause outside-in stripping of their molecular gas. On average, galaxies in the HERACLES sample have marginally smaller H_2 deficiencies and marginally larger H_2 radii. However, there is no statistically significant difference between both samples.

4.4. Central H_2 Surface Densities

Figure 5 shows the median surface density of the molecular gas disk as a function of H I deficiency (left-hand panel) and H_2 deficiency (right-hand panel), within a radius of $R = 0.1\,R_\star$ (typically corresponding to several hundred pc, roughly equivalent to the inner resolution element of the moment 0 map for most galaxies in the sample). This radius was chosen because, if any inward compression of the gas is taking place, the effect is likely subtle and primarily visible in the very center of the galaxy. While, by eye, there appears to be a weak correlation between H I deficiency and central H_2 surface density, it is not statistically significant (the Spearman correlation coefficient is $r_s = 0.26 \pm 0.05$ with a typical p value of 0.12).

There is no correlation between H_2 deficiency and central H_2 surface density (the Spearman correlation coefficient is $r_S = -0.18 \pm 0.09$, with a typical p value of 0.3). On average, galaxies in the HERACLES sample have marginally smaller H_2 deficiencies and marginally larger central H_2 surface densities. However, there is no statistically significant difference between both samples.

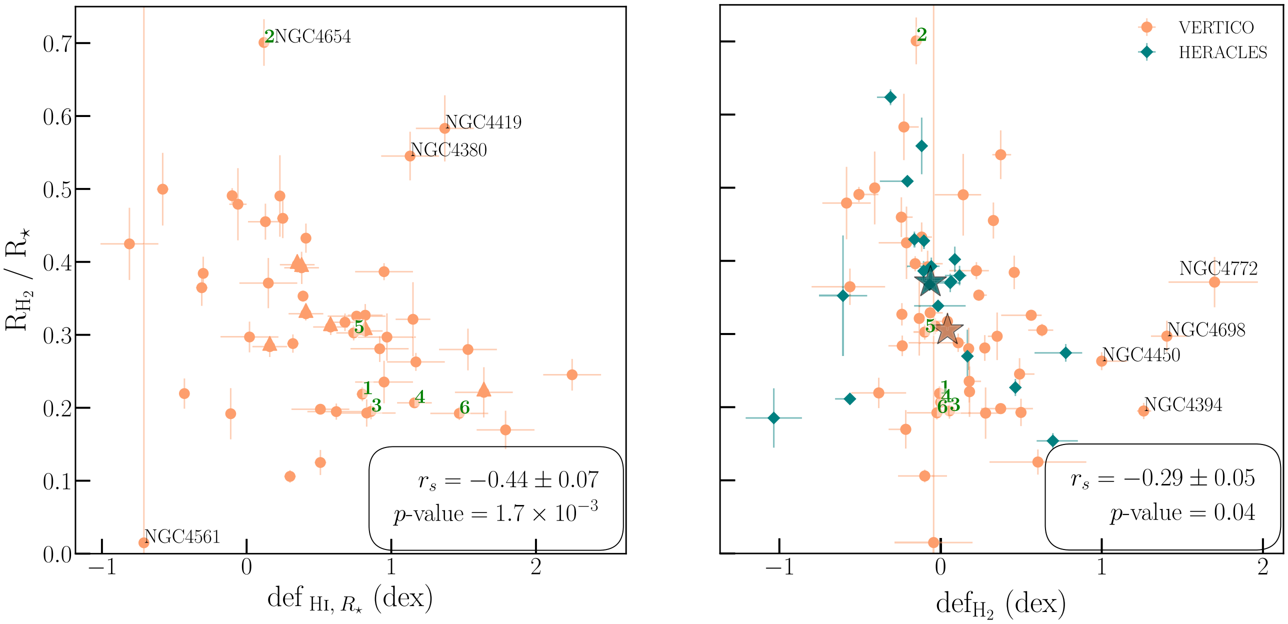

Figure 4. Radius of the molecular gas disk (normalized by the radius of the stellar disk) as a function of H I deficiency (left panel) and H_2 deficiency (right panel). Markers are the same as in Figure 1, but with the numbers indicating RPS galaxies now located to the upper right of the relevant markers. In the right-hand panel, the median values (both in x and y) of the VERTICO and HERACLES samples are indicated with orange and teal stars, respectively. The H_2 radius at an observed isodensity threshold of $\Sigma_{H_2} = 1\ M_\odot \mathrm{pc}^{-2}$ is plotted. There is an anticorrelation between H I deficiency and R_{H_2} (the Spearman correlation coefficient is $r_s = -0.44 \pm 0.07$ with a typical p value of 1.7×10^{-3}). The relation between H_2 deficiency and R_{H_2} at this isodensity threshold is weaker (the Spearman correlation coefficient is $r_S = -0.29 \pm 0.05$, with a typical p value of 0.04). H I deficiencies are associated with truncated H_2 disks, likely through outside-in stripping.

4.5. Effects of Definition of H_2 Radius

Figures 4 and 5 are shown for specific choices of the H_2 radius: in Figure 4, the radius of the H_2 disk is defined at $\Sigma_{H_2} = 1\ M_\odot\ \mathrm{pc}^{-2}$ and, in Figure 5, the median H_2 surface density is measured inside 0.1 $R_\star$. To investigate how the relationships shown in these plots change with the choice of radius (i.e., the isodensity threshold at which the H_2 radius is defined, and the semimajor axis of the ellipse enclosing the area in which the median H_2 surface density is calculated), we remake both figures using a number of different radii, and measure their Spearman correlation coefficients. Figure 6 shows these Spearman correlation coefficients for the relationships between H I deficiency (left-hand panel) and R_{H_2} and Σ_{H_2} (purple and orange, respectively), and, similarly, the relationships between H_2 deficiency and R_{H_2} and Σ_{H_2} (right-hand panel). Relationships for which the p value associated with Spearman's correlation is greater than 0.05 (and are thus considered to not be statistically significant) are indicated with semitransparent markers.

The relationship between H I deficiency and R_{H_2} is strongest for low isodensity thresholds, and disappears for higher thresholds. Thus, this correlation is only seen when the lower density material at the outskirts of the molecular gas disk is taken into account. The higher density material at smaller radii is not affected significantly. This implies either outside-in stripping, or the removal of molecular gas throughout the disk, resulting in the low-surface-density gas at the outskirts dropping below our detection threshold. However, the latter explanation would result in H_2 radial profiles with shapes similar to those of field galaxies, but scaled down, which is not observed for VERTICO galaxies (see Figure 3). The relationship between H_2 deficiency and R_{H_2} is present for all values of the isodensity threshold except the very highest, and is likely intrinsic.

The relationship between H I deficiency and Σ_{H_2} is not statistically significant, and any hint of increased H_2 surface densities is only present in the very centers of galaxies ($R < 0.1 R_\star$). The moderate negative correlation between H_2 deficiency and median H_2 surface density is independent of the choice of radius, although it is no longer statistically significant when the median H_2 surface density is calculated in the central regions only. This correlation is likely intrinsic.

5. Discussion

Globally, while H I deficiency only correlates weakly to moderately with H_2 deficiency, H I-deficient galaxies are often also H_2 deficient to varying degrees. This suggests that the environmental mechanisms acting on the H I in Virgo cluster galaxies simultaneously affect their H_2. However, the lack of a stronger correlation between both deficiencies, in combination with smaller H_2 deficiencies compared to H I deficiencies, implies that relatively little molecular gas has been removed from VERTICO galaxies. It is possible that H_2 deficiencies become more significant only after most of the H I is removed.

A closer look at the resolved properties of the molecular gas in these galaxies has revealed that absence of a strong correlation does not necessarily mean that the H_2 content of H I-deficient galaxies remains undisturbed by environmental process(es). Σ_{H_2} radial profiles of galaxies with larger H I deficiencies are more truncated and steeper than those of their more H I-rich counterparts, indicating outside-in removal of molecular gas. We explored this result in more detail by studying the radius and average surface density of the molecular gas disk as a function of both H I and H_2 deficiency. This has confirmed the presence of an anticorrelation between H I deficiency and the radius of the H_2 disk (Figure 4). This correlation is only significant when the low-density molecular gas at the outskirts of the disk is taken into account (Figure 6).

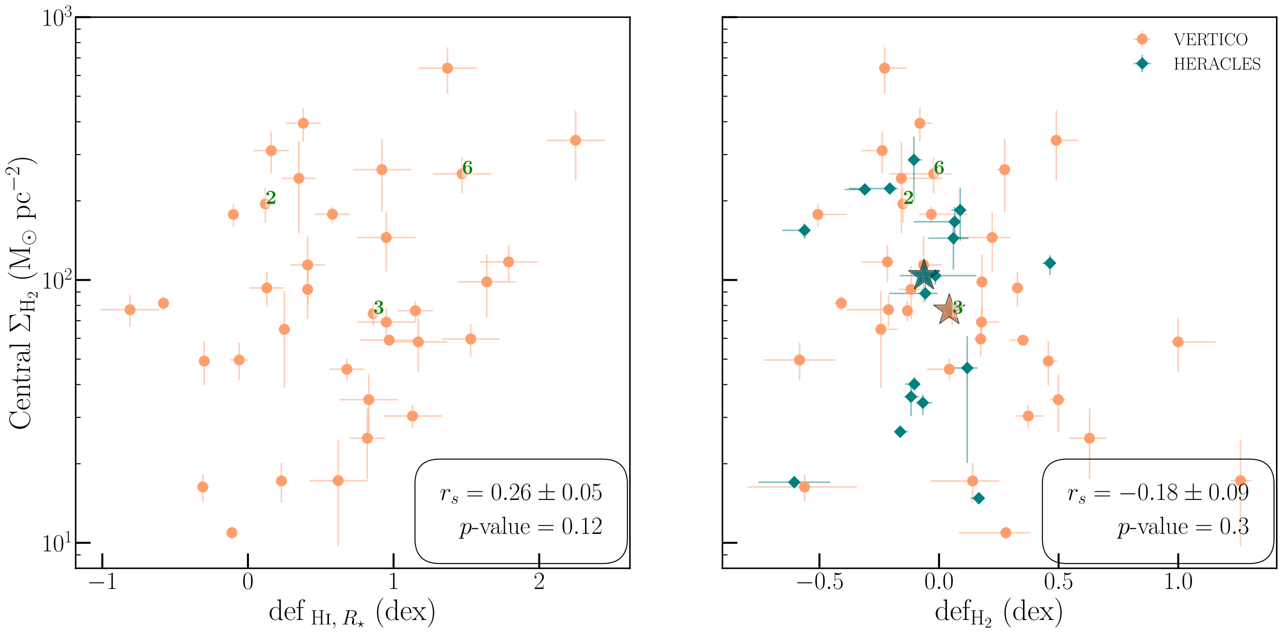

Figure 5. Similar to Figure 4, but showing median central H_2 surface densities within an ellipse with an observed semimajor axis of $0.1R_\star$ (e.g., the extreme centers of galaxies). While, by eye, there appears to be a weak correlation between H I deficiency and Σ_{H_2}, it is not statistically significant (the Spearman correlation coefficient is $r_S = 0.26 \pm 0.05$, with a typical p value of 0.12). There is no correlation between H_2 deficiency and Σ_{H_2} (the Spearman correlation coefficient is $r_S = -0.18 \pm 0.09$, with a typical p value of 0.3). VERTICO galaxies have central median H_2 surface densities similar to those HERACLES galaxies at similar def $_{H_2}$.

Furthermore, there is a hint of a slight increase in median central surface density ($R \lesssim 0.1R_\star$) of the H_2 disk with increasing H I deficiency, although this is not statistically significant. In this work, we have opted not to correct for inclination (see Section 3). The application of inclination corrections does not significantly alter the trends in any of the Figures, and therefore the broad conclusions of the paper remain the same with or without these corrections.

Our results partly agree with the results from Mok et al. (2017), who report steeper H_2 radial profiles of Virgo galaxies compared to those of galaxies in the field. They also find enhanced central surface densities, for which we do not find solid evidence here. Mok et al. (2017) mainly attribute this enhancement to radially inward migration of H I as a result of RPS, after which it is more easily converted to H_2. They also report increased global molecular gas masses of Virgo galaxies compared to field and group samples, which while here we mostly find H_2 deficiencies compared to main-sequence galaxies from xCOLD GASS. This difference is possibly the result of the use of an H I-mass-selected sample by Mok et al. (2017).

Our results also agree partly with those from Boselli et al. (2014a). While they indeed find an anticorrelation between H_2 radius and H I deficiency, they also report a strong correlation between H I and H_2 deficiency, whereas we find a weak correlation. The strong correlation between H I and H_2 deficiency found by Boselli et al. (2014a) is based on a subsample of 17 galaxies with high-quality data from Kuno et al. (2007). When the entire Virgo sample is taken into account, this relationship is not as strong (see Figure 5 in Boselli et al. 2014a). The range of H I deficiencies considered in this work is closer to that of the entire sample of Boselli et al. (2014a), rather than the subsample from Kuno et al. (2007). This subsample exclusively contains galaxies with H I deficiencies between ∼0 and 1, where the slope is steepest (Figure 2). Therefore, it is possible that the relationship found in this work is weaker because of the wider range of H I deficiencies, similar to Figure 5 of Boselli et al. (2014a). Uncertainties in X_{CO} and $R_{21} \equiv CO(2–1)/CO(1–0)$ may contribute to differences with previous work, although Boselli et al. (2014a) report a stronger correlation between H I and H_2 deficiency for a constant X_{CO}.

5.1. What Causes HI and H_2 Deficiencies?

Truncated molecular gas disks could be explained by several environmental mechanisms, such as RPS, tidal interactions, and galaxy-galaxy encounters. However, tidal interactions and galaxy-galaxy encounters are expected to result in significant kinematic in addition to morphological disturbances, which are not evident in the moment 1 maps of VERTICO galaxies (see Appendix A in B21). Thermal evaporation can remove gas from the disk, which could result in observed truncation as the surface density of the molecular gas at the outskirts of the disk drops below the sensitivity limit of our observations. The same is true for starvation. However, both of these processes should result in relatively uniform removal of gas, which should not significantly change the shape of the Σ_{H_2} radial profile. Additionally, the large amounts of hot ICM required for thermal evaporation would automatically result in RPS as satellite galaxies move through it.

The most likely explanation for the observed truncated molecular gas disks is RPS. In the earlier stages of RPS, the outer parts of the radial profile are likely dominated by the gas tail, resulting in a relatively flat and extended radial profile. It is possible that, as the stripping continues, the outer parts of the stripped tail become undetectable, resulting in a steeper and more truncated profile. Additionally, RPS could result in the inward compression of gas, which would contribute to the steepness of the Σ_{H_2} radial profiles, as also reported by, e.g., Mok et al. (2017).

Several moment zero maps of VERTICO galaxies exhibit clear RPS signatures (for example NGC4654; B21, Figure 4.22). If RPS is responsible for the truncation of the molecular gas disks, the lack of a stronger correlation between H I and H_2 deficiency suggests that it is not very effective at removing

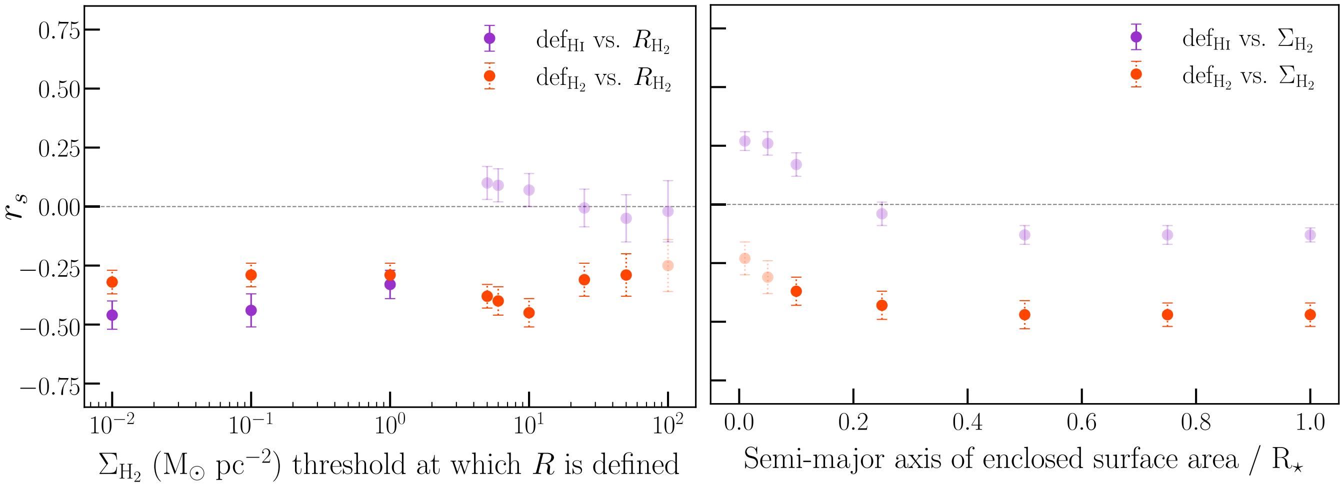

Figure 6. Left panel: Spearman correlation coefficients as a function of the observed isodensity threshold at which $R_{\mathrm{H_2}}$ is defined for the relationship between H I (purple) and H_2 (orange) deficiency and $R_{\mathrm{H_2}}$. Spearman test results with p values greater than 0.05 (i.e., relationships with no significant correlation) are indicated with semitransparent markers. There is an anticorrelation between $R_{\mathrm{H_2}}$ and both H I and H_2 deficiency. The anticorrelation between $R_{\mathrm{H_2}}$ and H I deficiency only exists if the isodensity radius of the H_2 disk is defined at low H_2 surface densities, i.e., the very outskirts of the disk. This is consistent with an outside-in stripping scenario of H_2 in H I-deficient galaxies. Right panel: Spearman correlation coefficients as a function of the observed semimajor axis of the ellipse in which the median H_2 surface density is calculated, for the relationships between H I (purple) and H_2 (orange) deficiency and H_2 surface density. There is an anticorrelation between H_2 deficiency and $\Sigma_{\mathrm{H_2}}$, which is likely intrinsic. Although there is a hint of slightly increased central H_2 surface densities, the relationship between H I deficiency and $\Sigma_{\mathrm{H_2}}$ is not statistically significant.

molecular gas from galaxies, or at least not in the early stages, when significant amounts of H I are still present. This is also reflected in Figure 2, which shows that the Virgo spirals with the clearest RPS signatures (including post-RPS peak galaxies) have relatively large H_2 fractions compared to other VERTICO galaxies with similar stellar masses. It is possible that only a small amount of low-density gas is stripped (at this stage).

One of the VERTICO galaxies with clear RPS signatures, NGC4402, has recently been studied in detail by Cramer et al. (2020) using high-resolution ($1'' \times 2''$, ∼80–160 pc at the distance of the Virgo cluster) CO(2 − 1) observations from ALMA. They estimate the strength of the ram pressure at the location of NGC4402 and find that only diffuse, low-surface-density H_2 (up to $2.5 - 10\,M_\odot\,\mathrm{pc}^{-2}$, depending on the exact ICM density at its location) can be stripped from this galaxy by RP. This limit is likely similar or lower for other galaxies in the VERTICO sample, as NGC4402 is probably close to the cluster center (∼0.4 Mpc in projection), and ram pressure decreases rapidly with cluster-centric radius ($p \propto r^{-2}$, Gunn & Gott 1972). This is in line with our findings, which suggest that RPS is acting on the molecular gas in VERTICO galaxies, but unable to remove significant amounts of it.

Cramer et al. (2020) also report a region with increased CO surface brightness as a result of RPS in NGC4402, resulting in enhanced star formation (which aids the removal of diffuse gas through stellar feedback). In a similar study of the CO in Coma cluster galaxy NGC 4921, Cramer et al. (2021) also find evidence for compression of the dense ISM on the leading side of this galaxy, accompanied by enhanced star-formation activity. As discussed above, similar results were found by Mok et al. (2017). Such increased molecular gas densities could explain the relatively large molecular gas fractions in well-studied RPS galaxies in the VERTICO sample (Figure 2), by offsetting the amount of diffuse H_2 lost through stripping. We do not find evidence for increased H_2 surface densities in this work. However, here we exclusively work with radially averaged radial profiles. More detailed (case) studies of the H_2 distribution and SFRs in VERTICO galaxies are needed to investigate how common regions with increased H_2 surface densities and star formation as a result of RPS are, and to what extent (and on what timescales) they can compensate the mass loss from the stripping of low-surface-density molecular gas.

Galaxies that do not show any sign of environmental effects on their H I reservoirs (class 0 galaxies in Yoon et al. 2017) are H_2 rich compared to galaxies that do. The difference in H_2 reservoirs between H I-normal and H I-disturbed objects confirms that the effects of environment on atomic gas also act on molecular gas. Galaxies with relatively low H I surface densities (class IV galaxies) are relatively H_2 poor. This suggests that (external or internal) processes resulting in lower gas surface densities are more effective at reducing the molecular gas reservoir than outside-in stripping. Galaxies with very strongly asymmetric and/or truncated H I disks cover a range in H_2 deficiencies, suggesting that the mechanisms causing these features do not necessarily significantly reduce the global molecular gas mass, at least on timescales where the galaxies still contain detectable H I.

Simulations of RPS acting on the multi-phase ISM (with H_2 treated as a separate component) have indeed shown that RPS can strip H_2 from the outer parts of galaxies, especially when the orientation of the wind is face-on (Lee et al. 2020). However, not all simulations agree on how molecular gas is impacted by RPS. Tonnesen & Bryan (2009) have shown, for example, that the fate of dense gas depends heavily on the strength of the RP: at low RP, the amount of high-density gas is enhanced, while it is depressed at high RPs. Similarly, Tonnesen (2019) find that, in recent infallers, compression can lead to high-density gas that is impossible to be stripped at later stages. Thus, whether significant amounts of H_2 are stripped, and whether H_2 is enhanced in galactic centers, likely varies between clusters, and depends on the locations of galaxies in phase space.

While simulations have rarely mapped H_2, some simulations show mild SF enhancement in RPS galaxies, particularly at the pericenter of their orbits (Bekki 2014; Steinhauser et al. 2016;

Ruggiero & Lima Neto 2017). However, not all of them agree on where in galaxies these enhancements are found. Tonnesen & Bryan (2012), Bekki (2014), and Boselli et al. (2021) find that SF in generally enhanced in the centers, while Roediger et al. (2014) find that SF is only enhanced via compression at the disk edges, right before gas is removed. All in all, there is little evidence for central enhancement of SF from simulations, and therefore, assuming that SF traces H_2, of central enhancement of H_2.

6. Summary

In this work we have investigated how environmental mechanisms acting on atomic gas affect the molecular gas in spiral galaxies in the Virgo cluster. Observations of 49 spiral galaxies in the Virgo cluster from the ALMA large program VERTICO: "the Virgo Environment Traced in CO" were used to study the resolved properties of the molecular gas. Their H I deficiencies, as well as deficiency/morphology classifications, were adopted from the VLA Imaging of Virgo in Atomic gas survey (VIVA, Chung et al. 2009; Yoon et al. 2017). In particular, we studied how the H_2 radial profile, radius, and surface density change as a function of H I deficiency, H_2 deficiency, and between different H I deficiency/morphology classes. Our main findings are as follows:

1. Many VERTICO galaxies that are H I deficient are also somewhat H_2 deficient, albeit to a lesser extent. There is a weak correlation between H I deficiency and H_2 deficiency, although it exhibits significant scatter. This suggests that, although environmental effects simultaneously affect H_2 and H I in VERTICO galaxies, H I deficiency does not always predict H_2 deficiency (i.e., when significant amounts of H I are removed from galaxies, they often still contain significant amounts of H_2).
2. Galaxies with larger H I deficiencies have steeper and less extended molecular gas radial profiles. This means that the mechanism removing atomic gas from galaxies causes truncation of the molecular gas disk.
3. We find an anticorrelation between H I deficiency and H_2 radius, which confirms that the environmental mechanisms removing atomic gas from galaxies remove or redistribute molecular gas from the outside in. This correlation is only significant when radius is measured at the outskirts of the H_2 disk, which implies that only the low-density gas at large radii is affected.
4. The most likely explanation for the observed steepened shapes of the Σ_{H_2} radial profiles of H I-deficient VERTICO galaxies is RPS, as other environmental processes are expected to result in the more uniform removal of H_2.
5. Galaxies that show clear signs of ongoing ram pressure stripping are H_2 normal to H_2 rich. This implies that RPS is not effective at reducing global molecular gas fractions on the timescales in which such features are still clearly visible.
6. Galaxies with low H I surface densities rather than asymmetries or truncation (class IV galaxies) are relatively H_2 poor. This suggests that additional external or internal mechanisms which reduce the gas density are more effective at reducing H_2 fractions than external processes causing outside-in stripping (i.e., RPS).

In summary, the atomic and molecular gas in VERTICO galaxies are affected by environment simultaneously. While H I deficiency is not a very accurate predictor of global H_2 deficiency, H I-deficient VERTICO galaxies show clear signs of outside-in removal of molecular gas.

This work was carried out as part of the VERTICO collaboration.

C.D.W. acknowledges support from the Natural Sciences and Engineering Research Council of Canada and the Canada Research Chairs program.

B.L. acknowledges support from the National Science Foundation of China (12073002, 11721303).

A.R.H.S. is a grateful recipient of the Jim Buckee Fellowship at ICRAR.

I.D.R. acknowledges support from the ERC Starting Grant Cluster Web 804208.

A.C. acknowledges the support from the National Research Foundation grant No. 2018R1D1A1B07048314.

K.S. and L.C.P. acknowledge support from the Natural Sciences and Engineering Research Council of Canada.

S.T. acknowledges support from the Simons Foundation.

L.C. acknowledges support from the Australian Research Council Discovery Project and Future Fellowship funding schemes (DP210100337, FT180100066). Parts of this research were conducted by the Australian Research Council Centre of Excellence for All Sky Astrophysics in 3 Dimensions (ASTRO 3D), through project number CE170100013.

V.V. acknowledges support from the scholarship ANID-FULBRIGHT BIO 2016-56160020, funding from NRAO Student Observing Support (SOS)-SOSPA7-014, and from partial support from NSF-AST1615960.

Parts of this research were supported by the Australian Research Council Centre of Excellence for All Sky Astrophysics in 3 Dimensions (ASTRO 3D), through project number CE170100013.

This work made use of HERACLES, 'The HERA CO-Line Extragalactic Survey (Leroy et al. 2009).

This paper makes use of the following ALMA data: ADS/JAO.ALMA# 2019.1.00763.L, ADS/JAO.ALMA# 2017.1.00886.L, ADS/JAO.ALMA# 2016.1.00912.S, ADS/JAO.ALMA# 2015.1.00956.S. ALMA is a partnership of ESO (representing its member states), NSF (USA) and NINS (Japan), together with NRC (Canada), MOST and ASIAA (Taiwan), and KASI (Republic of Korea), in cooperation with the Republic of Chile. The Joint ALMA Observatory is operated by ESO, AUI/NRAO and NAOJ. In addition, publications from NA authors must include the standard NRAO acknowledgment: The National Radio Astronomy Observatory is a facility of the National Science Foundation operated under cooperative agreement by Associated Universities, Inc.

Software:`Matplotlib` (Hunter 2007), `NumPy` (Harris et al. 2020), `Astropy` (Astropy Collaboration et al. 2013, 2018), `SciPy` (Virtanen et al. 2020), `Photutils` (Bradley et al. 2020), and `Lifelines` (Davidson-Pilon 2019).

Appendix
Additional figures

This Appendix contains additional Figures that are referred to at various points throughout the paper.

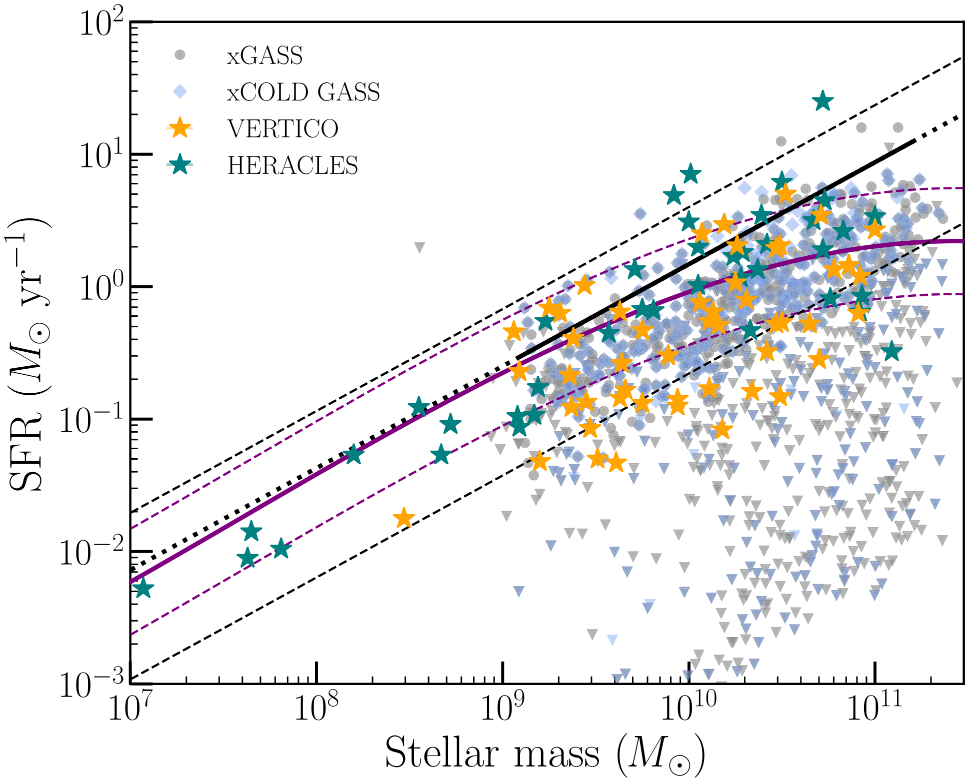

Figure A1. SFR–$M_\star$ plot for VERTICO (orange) and the control samples used in this work (xGASS in gray, xCOLD GASS in blue, and HERACLES in teal). Overlaid are the SFMS from Elbaz et al. (2007) in black (the thick, dotted line is an extrapolation of the solid line covering the stellar mass range in which the relationship was derived), and that from xCOLD GASS in purple (Saintonge et al. 2016). Stellar masses and star-formation rates for the x(COLD) GASS samples were adopted from GSWLC for consistency with VERTICO, for which they are adopted from z0MGS. Objects for which no 22 μm detection is available are indicated with down-pointing triangles. Following the style of Saintonge et al. (2016), error bars are omitted to improve readability. For the control sample used in this work, xGASS and xCOLD GASS galaxies within 2σ of the SFMS from Elbaz et al. (2007) are used, as indicated by the black dashed lines. While VERTICO and x(COLD) GASS are primarily scattered below the SFMS, HERACLES galaxies are distributed around higher SFRs. This is likely a result of selection.

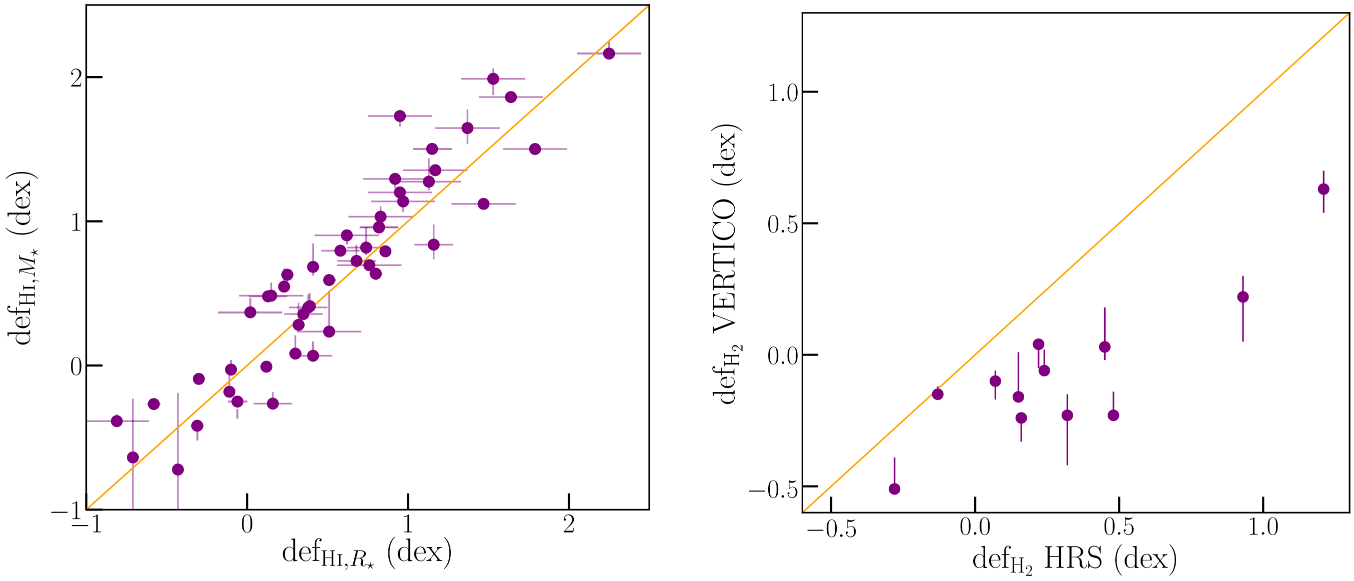

Figure A2. Left-hand panel: H I deficiencies of VERTICO galaxies from Chung et al. (2009), based on $R_\star$, vs. H I deficiencies based on the difference in H I fraction compared to field galaxies at fixed stellar mass (see Section 3.1 for their respective definitions). The orange line represents the one-to-one relation. H I deficiencies from Chung et al. (2009) correlate well with those based on H I fractions compared to the field. Right-hand panel: H_2 deficiencies for a subsample of VERTICO that overlaps with high-quality data from the HRS. H_2 deficiencies for the VERTICO sample are systematically smaller compared to those of the HRS, likely primarily because of the difference in control samples used to calibrate this parameter.

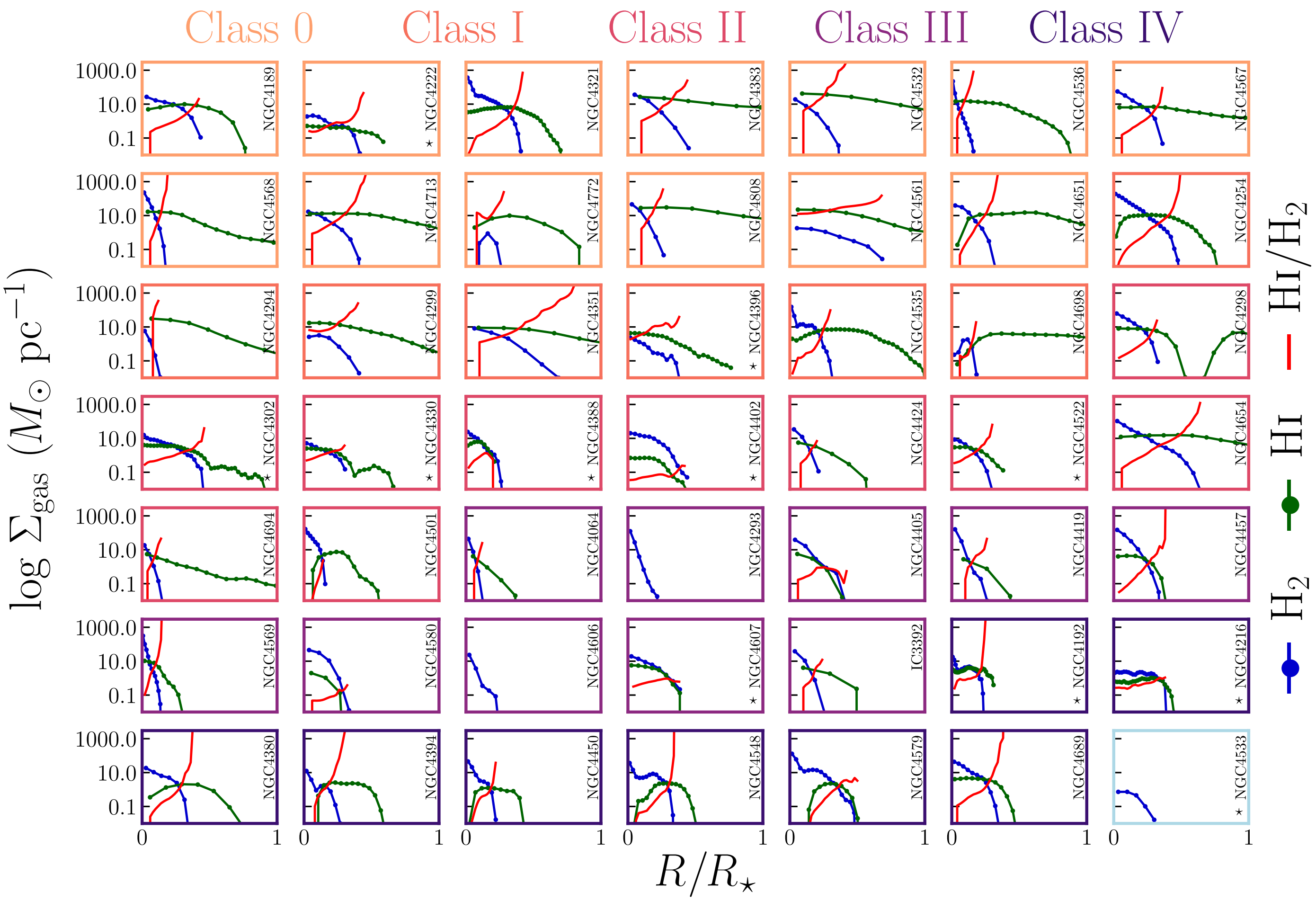

Figure A3. H_2 (blue) and H I (green) radial profiles of all 49 CO-detected galaxies in VERTICO. The profile of the H I-to-H_2 ratio is shown in red. The borders of the subplots are color-coded by the VIVA classification of the galaxy (see Section 3.6), indicated at the top of the figure (no class is available for NGC4533, see Section 3.6). Some galaxies (NGC4694, NGC4606, and NGC4293) only have marginal H I detections. Therefore, no reliable radial profiles could be made for them. NGC4533 was not detected in H I. Highly inclined galaxies (inc $\geqslant 80^o$) are indicated with a star in front of their name.

ORCID iDs

Nikki Zabel https://orcid.org/0000-0001-7732-5338
Toby Brown https://orcid.org/0000-0003-1845-0934
Timothy A. Davis https://orcid.org/0000-0003-4932-9379
Luca Cortese https://orcid.org/0000-0002-7422-9823
Alessandro Boselli https://orcid.org/0000-0002-9795-6433
Barbara Catinella https://orcid.org/0000-0002-7625-562X
Ryan Chown https://orcid.org/0000-0001-8241-7704
Aeree Chung https://orcid.org/0000-0003-1440-8552
Sara L. Ellison https://orcid.org/0000-0002-1768-1899
María J. Jiménez-Donaire https://orcid.org/0000-0002-9165-8080
Bumhyun Lee https://orcid.org/0000-0002-3810-1806
Kristine Spekkens https://orcid.org/0000-0002-0956-7949
Stephanie Tonnesen https://orcid.org/0000-0002-8710-9206

References

Accurso, G., Saintonge, A., Catinella, B., et al. 2017, MNRAS, 470, 4750
Alam, S., Albareti, F. D., Allende Prieto, C., et al. 2015, ApJS, 219, 12
Aniano, G., Draine, B. T., Gordon, K. D., & Sandstrom, K. 2011, PASP, 123, 1218
Astropy Collaboration, Robitaille, T. P., Tollerud, E. J., et al. 2013, A&A, 558, A33
Astropy Collaboration, Price-Whelan, A. M., Sipőcz, B. M., et al. 2018, AJ, 156, 123
Bekki, K. 2014, MNRAS, 438, 444
Binggeli, B., Sandage, A., & Tammann, G. A. 1985, AJ, 90, 1681
Bolatto, A. D., Wolfire, M., & Leroy, A. K. 2013, ARA&A, 51, 207
Boselli, A., Boissier, S., Cortese, L., et al. 2006, ApJ, 651, 811
Boselli, A., Boissier, S., Heinis, S., et al. 2011, A&A, 528, A107
Boselli, A., Casoli, F., & Lequeux, J. 1995, A&AS, 110, 521
Boselli, A., Cortese, L., Boquien, M., et al. 2014a, A&A, 564, A67
Boselli, A., Cuillandre, J. C., Fossati, M., et al. 2016, A&A, 587, A68
Boselli, A., Eales, S., Cortese, L., et al. 2010, PASP, 122, 261
Boselli, A., Fossati, M., Ferrarese, L., et al. 2018, A&A, 614, A56
Boselli, A., Fossati, M., Sun, M., et al. 2021, A&A, 646, A139
Boselli, A., Voyer, E., Boissier, S., et al. 2014b, A&A, 570, A69
Bradley, L., Sipőcz, B., Robitaille, T., et al. 2020, astropy/photutils: v1.0.0, Zenodo doi:10.5281/zenodo.4044744
Briggs, D. S. 1995, BAAS, 27, 1444
Brown, T., Wilson, C. D., Zabel, N., et al. 2021, ApJS, 257, 21
Catinella, B., Saintonge, A., Janowiecki, S., et al. 2018, MNRAS, 476, 875
Cayatte, V., van Gorkom, J. H., Balkowski, C., & Kotanyi, C. 1990, AJ, 100, 604
Chung, A., van Gorkom, J. H., Kenney, J. D. P., Crowl, H., & Vollmer, B. 2009, AJ, 138, 1741
Cortese, L., Catinella, B., & Smith, R. 2021, PASA, 38, e035
Cowie, L. L., & Songaila, A. 1977, Natur, 266, 501
Cramer, W. J., Kenney, J. D. P., Cortes, J. R., et al. 2020, ApJ, 901, 95
Cramer, W. J., Kenney, J. D. P., Tonnesen, S., et al. 2021, ApJ, 921, 22
Davidson-Pilon, C. 2019, JOSS, 4, 1317
Davies, J. I., Baes, M., Bendo, G. J., et al. 2010, A&A, 518, L48
Davis, T. A., Alatalo, K., Bureau, M., et al. 2013, MNRAS, 429, 5344
Dressler, A. 1980, ApJ, 236, 351
Elbaz, D., Daddi, E., Le Borgne, D., et al. 2007, A&A, 468, 33
Ferrarese, L., Côté, P., Cuillandre, J.-C., et al. 2012, ApJS, 200, 4

Fouqué, P., Solanes, J. M., Sanchis, T., & Balkowski, C. 2001, A&A, 375, 770
Fumagalli, M., Gavazzi, G., Scaramella, R., & Franzetti, P. 2011, A&A, 528, A46
Fumagalli, M., Krumholz, M. R., Prochaska, J. X., Gavazzi, G., & Boselli, A. 2009, ApJ, 697, 1811
Gavazzi, G., Boselli, A., Scodeggio, M., Pierini, D., & Belsole, E. 1999, MNRAS, 304, 595
Gavazzi, G., Boselli, A., van Driel, W., & O'Neil, K. 2005, A&A, 429, 439
Giovanelli, R., & Haynes, M. P. 1985, ApJ, 292, 404
Goto, T., Yamauchi, C., Fujita, Y., et al. 2003, MNRAS, 346, 601
Gunn, J. E., & Gott, J. R., III 1972, ApJ, 176, 1
Harris, C. R., Millman, K. J., van der Walt, S. J., et al. 2020, Natur, 585, 357
Haynes, M. P., & Giovanelli, R. 1984, AJ, 89, 758
Haynes, M. P., Giovanelli, R., & Chincarini, G. L. 1984, ARA&A, 22, 445
Herrera, C. N., Pety, J., Hughes, A., et al. 2020, A&A, 634, A121
Hughes, T. M., & Cortese, L. 2009, MNRAS, 396, L41
Hunter, J. D. 2007, CSE, 9, 90
Kenney, J. D. P., Geha, M., Jáchym, P., et al. 2014, ApJ, 780, 119
Kenney, J. D. P., & Young, J. S. 1989, ApJ, 344, 171
Kennicutt, R. C. J., Armus, L., Bendo, G., et al. 2003, PASP, 115, 928
Kennicutt, R. C., Jr 1998, ApJ, 498, 541
Kroupa, P., & Weidner, C. 2003, ApJ, 598, 1076
Kuno, N., Sato, N., Nakanishi, H., et al. 2007, PASJ, 59, 117
Larson, R. B., Tinsley, B. M., & Caldwell, C. N. 1980, ApJ, 237, 692
Lee, B., & Chung, A. 2018, ApJL, 866, L10
Lee, B., Chung, A., Tonnesen, S., et al. 2017, MNRAS, 466, 1382
Lee, J., Kimm, T., Katz, H., et al. 2020, ApJ, 905, 31
Leroy, A. K., Hughes, A., Liu, D., et al. 2021b, ApJS, 255, 19
Leroy, A. K., Sandstrom, K. M., Lang, D., et al. 2019, ApJS, 244, 24
Leroy, A. K., Schinnerer, E., Hughes, A., et al. 2021a, ApJS, 257, 43
Leroy, A. K., Walter, F., Bigiel, F., et al. 2009, AJ, 137, 4670
Leroy, A. K., Walter, F., Brinks, E., et al. 2008, AJ, 136, 2782
Lisker, T., Vijayaraghavan, R., Janz, J., et al. 2018, ApJ, 865, 40
Loni, A., Serra, P., Kleiner, D., et al. 2021, A&A, 648, A31
McLaughlin, D. E. 1999, ApJL, 512, L9
McMullin, J. P., Waters, B., Schiebel, D., Young, W., & Golap, K. 2007, in ASP Conf. Ser., 376, Astronomical Data Analysis Software and Systems XVI, ed. R. A. Shaw, F. Hill, & D. J. Bell (San Francisco, CA: ASP), 127
Mei, S., Blakeslee, J. P., Côté, P., et al. 2007, ApJ, 655, 144
Mihos, J. C., Harding, P., Feldmeier, J. J., et al. 2017, ApJ, 834, 16
Mok, A., Wilson, C. D., Golding, J., et al. 2016, MNRAS, 456, 4384
Mok, A., Wilson, C. D., Knapen, J. H., et al. 2017, MNRAS, 467, 4282
Moore, B., Katz, N., Lake, G., Dressler, A., & Oemler, A. 1996, Natur, 379, 613
Moretti, A., Paladino, R., Poggianti, B. M., et al. 2020, ApJL, 897, L30
NASA/IPAC Extragalactic Database (NED) 2019, https://ned.ipac.caltech.edu/
Nulsen, P. E. J. 1982, MNRAS, 198, 1007
Odekon, M. C., Koopmann, R. A., Haynes, M. P., et al. 2016, ApJ, 824, 110
Oemler, A., Jr 1974, ApJ, 194, 1
Rasmussen, J., Ponman, T. J., Mulchaey, J. S., Miles, T. A., & Raychaudhury, S. 2006, MNRAS, 373, 653
Roediger, E., Bruggen, M., Owers, M. S., Ebeling, H., & Sun, M. 2014, MNRAS, 443, L114
Ruggiero, R., & Lima Neto, G. B. 2017, MNRAS, 468, 4107
Saintonge, A., Catinella, B., Cortese, L., et al. 2016, MNRAS, 462, 1749
Saintonge, A., Catinella, B., Tacconi, L. J., et al. 2017, ApJS, 233, 22
Saintonge, A., Wilson, C. D., Xiao, T., et al. 2018, MNRAS, 481, 3497
Salim, S., Lee, J. C., Janowiecki, S., et al. 2016, ApJS, 227, 2
Schmidt, M. 1959, ApJ, 129, 243
Schröder, A., Drinkwater, M. J., & Richter, O. G. 2001, A&A, 376, 98
Solanes, J. M., Manrique, A., García-Gómez, C., et al. 2001, ApJ, 548, 97
Solanes, J. M., Sanchis, T., Salvador-Solé, E., Giovanelli, R., & Haynes, M. P. 2002, AJ, 124, 2440
Solomon, P. M., & Vanden Bout, P. A. 2005, ARA&A, 43, 677
Stark, A. A., Knapp, G. R., Bally, J., et al. 1986, ApJ, 310, 660
Steinhauser, D., Schindler, S., & Springel, V. 2016, A&A, 591, A51
Tonnesen, S. 2019, ApJ, 874, 161
Tonnesen, S., & Bryan, G. L. 2009, ApJ, 694, 789
Tonnesen, S., & Bryan, G. L. 2012, MNRAS, 422, 1609
Verheijen, M. A. W., & Sancisi, R. 2001, A&A, 370, 765
Virtanen, P., Gommers, R., Oliphant, T. E., et al. 2020, NatMe, 17, 261
Vollmer, B. 2003, A&A, 398, 525
Vollmer, B. 2009, A&A, 502, 427
Vollmer, B., Balkowski, C., Cayatte, V., van Driel, W., & Huchtmeier, W. 2004, A&A, 419, 35
Vollmer, B., Braine, J., Pappalardo, C., & Hily-Blant, P. 2008, A&A, 491, 455
Vollmer, B., Soida, M., Braine, J., et al. 2012, A&A, 537, A143
Walter, F., Brinks, E., de Blok, W. J. G., et al. 2008, AJ, 136, 2563
Waugh, M., Drinkwater, M. J., Webster, R. L., et al. 2002, MNRAS, 337, 641
Yoon, H., Chung, A., Smith, R., & Jaffé, Y. L. 2017, ApJ, 838, 81
York, D. G., Adelman, J., Anderson, J. E. J., et al. 2000, AJ, 120, 1579
Zabel, N., Davis, T. A., Smith, M. W. L., et al. 2019, MNRAS, 483, 2251